

# Computer Simulation of the Early and Late Stages of the Self-Assembly of ZIF-8

Salvador R. G. Balestra<sup>1,2,3</sup> and Rocio Semino\*<sup>1</sup>

<sup>1</sup>ICGM, Univ. Montpellier, CNRS, ENSCM, Montpellier, France

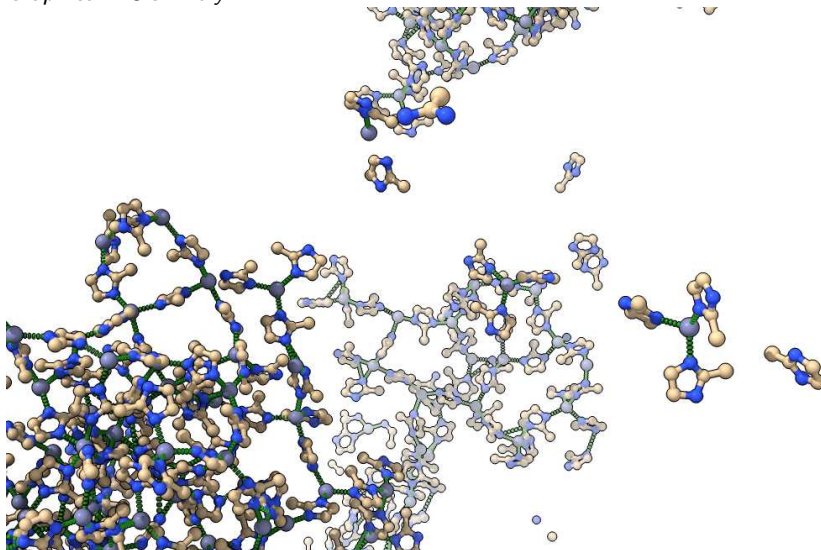
<sup>2</sup>Departamento de Sistemas Físicos, Químicos y Naturales, Universidad Pablo de Olavide, Ctra. Utrera km 1, Seville ES-41013, Spain

<sup>3</sup>Instituto de Ciencia de Materiales de Madrid, Consejo Superior de Investigaciones Científicas (ICMM-CSIC) c/Sor Juana Inés de la Cruz 3, Madrid ES-28049, Spain

## Abstract

We employ well-tempered metadynamics simulations to study the mechanistic details of both endpoints of the self-assembly process of the benchmark metal-organic framework ZIF-8: the early stages of nucleation and crystal decomposition. To do so, we developed and validated a force field that reliably models the modes of coordination bonds via a Morse potential functional form and employs cationic and anionic dummy atoms to capture coordination symmetry. We also explored a set of physically relevant collective variables and carefully selected an appropriate subset for our problem at hand. After a rapid increase of the Zn-N connectivity, we observe the evaporation of small clusters in favour of a few large clusters, that lead to the formation of an amorphous highly-connected aggregate.  $Zn(MIm)_4^{2-}$  and  $Zn(MIm)_3^-$  complexes are observed, with lifetimes in the order of a few picoseconds, while larger structures, such as 4-, 5- and 6-membered rings, have substantially longer lifetimes of a few nanoseconds. The free ligands act as “templating agents” for the formation of the sodalite cages. ZIF-8 crystal decomposition results in the formation of a vitreous phase. Our findings contribute to a fundamental understanding of MOF’s synthesis that paves the way to controlling synthesis products. Furthermore, our developed force field and methodology can be applied to model solution processes that require coordination bond reactivity for other ZIFs besides ZIF-8.

Graphical TOC Entry:



**Keywords:** Metadynamics, Metal-Organic Frameworks, Building Blocks, Self-Assembly, Collective Variables, Nucleation Modelling

## Introduction

Metal-Organic Frameworks (MOFs) have revolutionised research in the fields of clean energy, environment and health due to their wide variety both in terms of chemical composition and topology, which confer them a vast array of shape-, selectivity-, reactivity- and confinement-

based properties. Indeed, MOFs can be formed by most of the existing metals in the periodic table in the form of cations or metal-based clusters combined with a large variety of organic polydentate ligands such as carboxylates, phosphonates and imidazolates, and they can exhibit many different pore shapes and sizes.<sup>1</sup> Thus, they constitute the ideal playground for synthesis scientists to create new porous materials with societally relevant applications, including water and food treatment, carbon capture, cata-

\*rocio.semino@umontpellier.fr

lysis and drug delivery.<sup>2–8</sup> Even though researchers have both achieved a good understanding of structure/property relationships for MOFs<sup>9–14</sup> and mastered several MOF synthesis techniques,<sup>15</sup> MOF rational design is still in its infancy. Only a few valuable efforts have led to establishing some principles for the rational design of MOF synthesis based on coordination and reticular chemistry.<sup>16–20</sup> A deeper understanding of the mechanisms underlying MOF self-assembly would undoubtedly make a leap in the quest for MOF rational design.

While a few experimental studies have addressed the crystal growth of MOFs by various *ex situ* and *in situ* analytical techniques, including HRTEM, EDXRD and diverse spectroscopies,<sup>21–30</sup> the required resolution to fully understand this complex process at the molecular-level cannot yet be experimentally achieved, that is, the association of the ligands with the cationic moieties to form oligomeric aggregates in solution leading to the formation of the first secondary building units (SBUs) and beyond. From the modelling standpoint, only a handful of studies have been devoted so far to the simulation of the pre-nucleation process of MOFs in solution. Yoneya *et al.*<sup>31</sup> modelled the first stages of polymerisation between  $\text{Ru}^{2+}$  and  $\text{Pd}^{2+}$  and 4,4'-bipyridine by means of classical molecular dynamics (MD) simulations considering an implicit solvent model. Biswal and Kusalik<sup>32</sup> then applied the same methodology to model the polymerisation between  $\text{Zn}^{2+}$  and 1,4-benzenedicarboxylic acid ligands including an explicit solvent model, and further studied the effect of the complexity of the chosen model on the results.<sup>33</sup> Despite the fact that the importance of the force field was clearly demonstrated in this latter study, no special efforts were dedicated to the development and validation of force fields to model MOF self-assembly up to date. These studies have introduced the use of cationic dummy atoms (CDA) models,<sup>34</sup> in order to better represent the anisotropic electronic density distribution when the metal cation is exposed to a field generated by the organic ligands to reproduce the correct topology of the final material.

The above mentioned studies described the formation of amorphous aggregates comprising the inorganic and organic moieties in solution, but no signs of the onset of crystallisation were observed. This is not surprising, since the collective motions that are required to achieve local order constitute rare events, which are only very seldom sampled in a regular MD simulation. It is only by the use of enhanced sampling techniques that these energy barriers may be overcome in a statistically meaningful fashion. Colón *et al.*<sup>35</sup> were able to obtain a cluster-like ordered structure by means of Finite Temperature String methods. Following the same philosophy, Kollias *et al.*<sup>36</sup> applied metadynamics<sup>37</sup> simulations to the study of the early stages of the nucleation of MIL-101(Cr) starting from half SBUs, and made a step forward by also considering the ionic force effects by means of the explicit inclusion of counterions. This latter work was a follow up of a previous *ab initio* investigation of the mechanism of formation of MIL-101(Cr) SBUs.<sup>38</sup> Recently, Filez *et al.*<sup>39</sup> combined density functional theory (DFT) calculations and MD simulations with *in situ* elastic scattering

and mass spectroscopy to unveil molecular-level details of the mechanism of the first stages of the nucleation of ZIF-67, a  $\text{Co}^{2+}$  sodalite MOF. They describe the metal-ligand complexes that are formed in solution upon addition of the ligand as well as the associated  $\text{Oh} \rightarrow \text{Td}$  symmetry changes and their lifetimes and give additional evidence to the hypothesis of the existence of an amorphous intermediate species along the self-assembly process.

In this contribution we build on these previous works by studying both endpoints of the nucleation process, namely (a) the early stages of self-assembly of metal ions and organic ligands and (b) the decomposition of a pre-formed MOF crystal, by Well-Tempered Metadynamics (WT-MetaD) simulations.<sup>39,40</sup> We introduce several methodological improvements to previous works: (i) a more physically sound force field that treats the metal-ligand interaction with a Morse potential instead of a Lennard-Jones or a harmonic potential as was the case in previous works (ii) a robust force field validation, and (iii) a comprehensive exploration of the suitability of different collective variables for the study of nucleation.<sup>41–43</sup> We apply our simulation method to the elucidation of the early and late stages of the self-assembly of the archetypal MOF ZIF-8<sup>44</sup> (ZIF stands for Zeolitic Imidazolate Framework), that features many applications<sup>45</sup> and whose growth has been well studied from an experimental point of view.<sup>23,26,28,29</sup> ZIF-8 is formed by  $\text{Zn}^{2+}$  cations tetrahedrally coordinated to 2-methylimidazolate ( $\text{MIm}^-$ ) ligands forming a sodalite topology. Many synthesis routes are reported in the scientific literature for this material, both as a powder or as a membrane/film.<sup>45,46</sup> In what follows, we will concentrate on solvent-based syntheses. ZIF-8 has been synthesised in water,<sup>47</sup> methanol ( $\text{MeOH}$ ),<sup>48</sup> Dimethylformamide (DMF),<sup>44</sup> and Dimethyl sulfoxide (DMSO),<sup>49</sup> among other solvents. Changing the solvent has been shown to modify the size and morphology of the obtained crystals,<sup>49</sup> which may influence the properties of the resulting material.<sup>50</sup> Besides the solvent, the metal to ligand ratio can also affect the result of the synthesis.<sup>47</sup> This plethora of synthesis works illustrates the complexity of ZIF-8's crystal growth.

We make a leap forward in the understanding of the self-assembly of ZIF-8 in this contribution. We shed light into molecular-level mechanistic details such as: (i) the nature and lifetimes of the different chemical species that can be found in solution at the early stages of self assembly, (ii) the role of the ligands as templating agents for the formation of sodalite cages, (iii) the formation of an intermediate highly connected amorphous aggregate and (iv) the height of the free energy barriers associated both to the ZIF-8 crystal decomposition and to the formation of the amorphous intermediate species. Our results provide support to mechanistic hypothesis that had been proposed by previous researchers<sup>51</sup> and give further insight for the first time.

This paper is structured as follows. In Section 1, we present the force field, its validation and the collective variables used in the MD simulations, along with a detailed discussion on why we chose them. Section 2 is devoted to the analysis and rationalisation of the simulations results. Our main conclusions are summarised in

section 3.

## 1 Methodology

### 1.1 Simulation Details

The Large-scale Atomic/Molecular Massively Parallel Simulator (LAMMPS)<sup>52</sup> code was used to perform all the simulations. Energy optimisations were calculated using a self-consistent cycle at each step of the minimisation, where the cell volume and shape were anisotropically relaxed using the Polak and Ribi  re<sup>53</sup> version of the conjugate gradient algorithm followed by an optimisation of the atomic positions using the damped dynamics method described by Bitzek *et al.*<sup>54</sup> MD simulations were run in the NPT ensemble using the Nos  -Hoover thermostat with a timestep of  $dt = 0.5$  fs. Thermostat and barostat relaxation times were set to  $10dt$  and  $100dt$ , respectively. The Ewald summation method was used to calculate the electrostatic contribution to the energy.

The initial coordinates of the reactive species were generated as follows: a) NVT Monte Carlo (MC) simulations were performed using the RASPA code,<sup>55</sup> for those systems starting from a completely uncoordinated phase (that is the solvated metal cation and ligands), and b) the experimental crystallographic coordinates were subsequently geometry optimised *via* the LAMMPS code for systems starting from a crystalline phase. In both cases the solvent coordinates were generated *via* a subsequent NVT MC simulation. For the simulations starting from the crystalline phase, the dummy atoms were added to the structure by means of a in-house program written in FORTRAN. The LAMMPS inputs were automatically generated from the coordinates obtained from the NVT MC simulation by another in-house program written in FORTRAN. Both have been added to the Supplementary Information and uploaded to a publicly available online repository: <https://github.com/salrodgom/ZIFWTMetaDnbZIFFF>. The WT-MetaD simulations were performed with the multiple walker enhanced sampling technique, using 6 walkers that were run with 32 cores each.

For the WT-MetaD simulations performed to study the polymerisation of  $Zn^{2+}$  and  $MIIm^-$  moieties, we tested systems of different sizes, namely 12, 96, and 324  $Zn^{2+}$  cations. In all simulations, the charge was neutralised with  $MIIm^-$  anions in a stoichiometric proportion. In these cases, we have kept the explicit solvent (MeOH) molecules- $Zn^{2+}$  ratio constant and equal to  $128/3$ , which corresponds to the loading of MeOH in ZIF-8 calculated from  $\mu$ VT MC simulations at 1 bar and 298 K.

The initial atomic positions for the ZIF-8 crystal were taken from Park *et al.*<sup>44</sup> and a  $2 \times 2 \times 2$  supercell was built from them.

Table 1 lists the simulation experiments that were conducted.

### 1.2 nb-ZIF-FF force field development

To the best of our knowledge, Hu *et al.*<sup>56</sup> developed the first ZIF-8 force field, which was later updated by

Zhang *et al.*<sup>57</sup> Since then, several groups have developed new models to reproduce ZIF-8's experimentally observed properties, such as its mechanoelastic behaviour, its infrared spectrum and the *flapping* of ligands in the pore windows, among others.<sup>58-61</sup> All these force fields treat the interaction between the coordination centres, namely the  $Zn^{2+}$  cations, and the nitrogen N atom of the ligand with a bonded potential, which precludes modelling bond breaking and formation. Since taking into account the bond formation and breaking equilibrium is essential for studying self-assembly processes, we have developed a new force field: nb-ZIF-FF (nb stands for non-bonded). The intramolecular, electrostatic and van der Waals interactions of our force field are based on the force field by Weng and Schmidt also called ZIF-FF.<sup>60</sup> We discarded all the bonds, angles and torsions that imply Zn–N contacts and replaced them by a Morse functional form, which is known to capture the coupled motion of coordination bonds. In addition, the spatial orientation of the  $Zn^{2+}$ —N<sup>–</sup> dipoles needs to be considered to achieve the correct ZIF-8 topology.

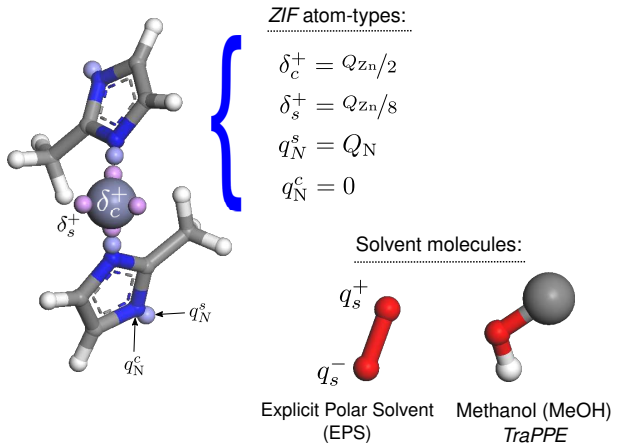


Figure 1: Scheme of the cationic and anionic dummy-atom models for  $Zn^{2+}$  ( $\delta_s^+$  and  $\delta_c^+$  shell and core particles, respectively),  $MIIm^-$  ( $N^s$  and  $N^c$ , shell and core particles for N atoms) as well as the two explicit solvent models that were considered in nb-ZIF-FF. N, C, H, Zn, O and the dummy particles are shown in blue, grey, white, light purple, red and pink/cyan, respectively. The Methyl group in MeOH is represented by a large grey sphere.

For this, we rely on CDA models for the metallic cations  $Zn^{2+}$ , as well as for the  $MIIm^-$  ligand moiety (see Figure 1). The CDA model,<sup>34</sup> as well as the electrostatic interactions between the different dummy atoms, will play a central role in modelling the directionality of the organic ligand assembly around the metal cation in the absence of angle and torsion interactions, as shown by Jawahery *et al.*<sup>62</sup> Within our CDA model, a central particle with charge  $q_{Zn}^c$  is surrounded by four other charged particles, the shell dummies, with charges  $q_{Zn}^s$ , each of them placed in one of the four vertexes of a tetrahedron centred in the central particle. The distance between shell and central particles is 0.9   . The total sum of the charges is equal to the charge assigned to the  $Zn^{2+}$  cation in the model by Weng and Schmidt,<sup>60</sup>  $Q_{Zn} = q_{Zn}^c + 4q_{Zn}^s = 0.7072$  e.

Table 1: Simulation experiments that were carried out in this work.

Initial condition	Cell Size	Type	T / K	Solvent	Zn <sup>2+</sup> & solvent numbers
ZIF-8 crystal	2 × 2 × 2	Unbiased MD	300, 450, 600, 800, and 1000	MeOH	96 and 400
ZIF-8-like cluster	~ 68 Å	Unbiased MD	298	EPS	442 and 6864
Solvated Zn <sup>2+</sup> and MIm <sup>−</sup>	~ 33 Å	WT-MetaD	300, 370, 450	MeOH	12 and 512
	~ 67 Å				96 and 4096
	~ 100 Å				324 and 13824
ZIF-8 crystal	2 × 2 × 2	WT-MetaD	300, 450	MeOH	96 and 400 96 and 300 96 and 447

While the central particle interacts *via* a sum of the Morse-based dispersion and Coulombic potentials, the shell atoms are only involved in electrostatic interactions. In addition, we have modelled the N atoms by a two sites anionic dummy atom model: a dummy particle containing all the N charge  $Q_N = q_N^s$ , was introduced at a distance of 0.5 Å from the original particle modelling N, which is located at the atom's position within the MIm<sup>−</sup> cycle and only interacts through dispersion interactions modelled *via* the Morse potential. The charge distribution was chosen so as to reproduce the radial distribution functions and other structural properties in crystalline ZIF materials (see Section 1.3 and Supporting Information (SI), Section S2). The original harmonic potential considered by Weng and Schmidt<sup>60</sup> for modelling bonded contributions has the electrostatic interaction embedded within, we took this into account when parameterising our Morse potential. A detailed explanation of the potential fitting process, as well as some additional details related to the force field are given in the SI (see Section S2).

Even though nb-ZIF-FF was exclusively applied to model ZIF-8 in the context of this work, we note that it can also be applied to model other ZIFs, as discussed in the validation section 1.3. Indeed, we have calculated different structural and energetic properties of many ZIFs using nb-ZIF-FF and obtained excellent results compared to experimental and first principles calculations data as shown in Table 2.

The solvent was treated *via* three different force field models: an implicit and two explicit ones. Implicit solvent models allow to sample much longer MD simulations times,<sup>63</sup> while an explicit solvent is necessary to study the collaborative mechanisms between solvent and reactants during the nucleation process.<sup>32,33</sup> For the implicit solvent, we have employed a corrected Coulomb interaction in which the dielectric permittivity,  $\epsilon$ , is distance dependent. At short distances the relative permittivity tends to a dielectric saturation value  $\epsilon_c$  —close to vacuum—, while at long distances the relative permittivity reaches its bulk limit:  $\epsilon_r \rightarrow 78.2$ , which corresponds to the value for water. To model the solvation shell around the inorganic and organic moieties, a small potential barrier has been added to frustrate a certain number of attempts of metal-ligand approaches, thus mimicking the role of the solvent in the early stages of nucleation, as in the work by Nguyen and Grünwald.<sup>63</sup> We have used the implicit solvent model

in preliminary work to set up the input files to study the WT-MetaD simulations and to explore the behaviour of different collective variables at a reduced computational cost. All simulation results that we report come from the explicit solvent simulations. Most of these have been carried out by considering the united atoms TraPPE<sup>64</sup> force field model for Methanol (MeOH). The interatomic cross interactions between the solvent and the nucleating species were modelled by LJ potentials whose parameters were calculated by applying the Lorentz-Berthelot mixing rules. The third and final solvent model considered only for force field validation calculations was a simple dipole proposed by Biswal and Kusalik,<sup>33</sup> labelled EPS (from Explicit Polar Solvent) in Table 1 (see Figure 1).

### 1.3 nb-ZIF-FF Validation

nb-ZIF-FF has been carefully validated by testing it against a set of relevant structural and energetic properties compared with those obtained from experimental and first principles calculations data, namely: *a*) the structural stability of the crystalline geometries of a series of ZIFs as well as of *b*) a solvated nanocluster of ZIF-8 at 298 K and *c*) the structural and geometric parameters as well as *d*) the elastic constants for a series of ZIFs.

Dürholt *et al.*<sup>61</sup> and Lewis *et al.*<sup>65</sup> have computed the energies of a series of highly stable ZIFs *via ab initio* calculations. They have predicted that the energies follow the trend:  $E_{zni} < E_{cag} < E_{BCT} < E_{MER} < E_{SOD} < E_{DFT} < E_{GIS}$ . We computed the energy relative to  $E_{zni}$  for the same ZIFs subset using nb-ZIF-FF, and found that the trend is quite well reproduced:  $E_{zni} < E_{cag} < E_{BCT} < E_{DFT} < E_{SOD} < E_{MER} < E_{GIS}$ . A table with the energies can be found in the SI (Table S2). The most significant difference is in the relative energy of the DFT structure. We believe that this is due to the fact that DFT presents two types of Zn-Ligand-Zn angles that nb-ZIF-FF is not able to resolve, since it has no bending terms to account for them. This is not a problem for our current work, since we are using this force field to model the self-assembly of ZIFs and not the crystalline materials themselves. Because most of these structures are composed by Imidazolate ligands (instead of MIm<sup>−</sup>), we added some new atom types to the force field to adapt it. These are minor changes, that do not modify the force field in its essence, more information can be found in the

To further probe the nb-ZIF-FF force field, we determined the cell parameters for the series of ZIFs mentioned above as well as for ZIF-8 and compared them to experimental, *ab initio*- and force field-based calculations data. The results are presented in Table S1. We observe a good agreement between the nb-ZIF-FF calculated and experimental cell parameters. Our calculations are also consistent with both previously published force field- and electronic structure-based calculations.<sup>61,65</sup>

We further put our force field to test by assessing the structural stability of a ZIF-8 nanocluster (see Figure 2a), for which the surface exposed to the solvent represents roughly 25% of the material. The cluster was built by cropping a periodic  $3 \times 3 \times 3$  ZIF-8 structure and it was inserted into a  $a = 100 \text{ \AA}$  cubic simulation box. Because the clean cuts of periodic systems lead to unrealistic surfaces, some extra surface elements ( $\text{MIm}^-$  and  $\text{Zn}^{2+}$ ) were added to minimise the surface electric charges. The cluster was immersed in the EPS solvent proposed by Biswal and Kusalik,<sup>33</sup> such that the system contained 442  $\text{Zn}^{2+}$ , 884  $\text{MIm}^-$  and 6864 EPS molecules. The snapshot shown in Figure 2a was collected after 5 ns of MD simulation at 298 K and it shows that the sodalite cages of the ZIF-8 nanocluster maintain their shape. Interestingly, we observed that some  $\text{MIm}^-$  ligands at the cluster surface are dissociated and adsorbed and some  $\text{Zn}^{2+}$  cations are almost completely surrounded by solvent molecules. The same behaviour was observed during the self-assembly simulations that will be detailed in Section 2.

We also computed the pair-correlation functions  $g(r)$  between Zn–N and Zn–Zn atoms. Figures 2b and 2c show that there is a good agreement between nb-ZIF-FF predictions, those by ZIF-FF and the experimental values measured by Cao *et al.*<sup>68</sup> and Bennett *et al.*<sup>69</sup> The distances of the first maximum and minimum for Zn–N are 2.0  $\text{\AA}$  and 3.0  $\text{\AA}$ , respectively, and for Zn–Zn pairs are 6.0  $\text{\AA}$  and 7.5  $\text{\AA}$  respectively. Pair correlation functions during a pre-nucleation stage from a nb-ZIF-FF unbiased MD simulation in the canonical ensemble at 298 K are also shown (cyan line in Figures 2b and 2c). The first peak is displaced to larger distances for low degrees of polymerisation (which can be correlated to less Zn–N bonds and more MeOH–Zn and MeOH–N interactions). This highlights the central role of the solvent in the self-assembly process. In addition, the Zn–N  $g(r)$  corresponding to several other ZIFs crystal structures are reported in the SI (see Figure S5). All of them show values that are in good agreement with the experimentally-measured ones.

As a final stringent validation criterion, we computed the elastic constants for our selected series of ZIFs. SOD ZIFs results are presented in Table 3 while those for the rest of the ZIFs are shown in the SI. The agreement between our elastic constant calculations and the experimental/calculated values is excellent.

All of the above validation tests give us confidence to pursue the study of the self-assembly of ZIF-8 considering nb-ZIF-FF as a reliable force-field.

## 1.4 Sampling of nucleation events

Since MOF nucleation is an activated process, the events that lead to it are rarely sampled in a molecular dynamics simulation and the ergodic hypothesis is not fulfilled. In this work, we tackle this problem by relying on the multiple-walkers<sup>72</sup> Well-Tempered Metadynamics<sup>39</sup> enhanced sampling method. To briefly illustrate how WT-MetaD works, let us consider a couple of functions of the atomic coordinates that adequately describe the nucleation process in a low-dimensional space. These functions are usually called collective variables (CVs),  $s(q)$ , and they allow to distinguish between the different states associated to the local free energy minima that characterise the physically relevant portion of the free energy surface. In WT-MetaD,<sup>39</sup> a history-dependent bias potential that drives the system evolution along the CVs is added to the Hamiltonian. This potential is defined such that energy penalties in the form of Gaussians are periodically deposited over the free energy surface in the CVs space, thus reducing the probability of revisiting configurations that have already been sampled. The rate of deposition of this bias potential decreases over the simulation time. The probability distribution sampled by the biased system is given by:

$$P_{\text{WT-MetaD}}(s(q)) \propto P(s(q))^{\frac{1}{\gamma}} \quad (1)$$

where  $P(s(q))$  is the probability distribution sampled in the isothermal–isobaric ensemble and  $\gamma = T + \Delta T / T$ .  $\gamma$  is chosen as an estimate of the height of the free energy barrier between the relevant states.<sup>40</sup> Here, we estimated the height of the barrier based on the results of an *in situ* XRD study performed by Cravillon *et al.*<sup>73</sup> The authors estimated the nucleation rate constants in the 393 K to 413 K temperature range by fitting crystallisation data with the Gualtieri equation for solvothermal syntheses carried out in MeOH. They subsequently estimated the activation energy of nucleation from an Arrhenius plot  $E_a = 69 \text{ kJ mol}^{-1}$ , then  $\gamma(400 \text{ K}) = \frac{8300 \text{ K}}{400 \text{ K}} \sim 20$ . We thus chose  $\gamma = 20$  for our simulations at  $T = 400 \text{ K}$ . We also explored other values, namely  $\gamma = 3, 10, 40$ . We considered a height of  $2k_B T$  for the deposited Gaussians. The width was estimated for each CV by running unbiased MD simulations and computing the standard deviation of the CVs distribution.

CV selection can be very challenging as a poor choice of CVs can prevent the free energy calculation from converging.<sup>40</sup> For this reason, we decided to systematically explore different CVs, including the simulation box volume, the enthalpy, the connectivity and local- and long-range-order parameters. In the following paragraphs we will provide a short explanation of each of the CVs. Two connectivity-related CVs were considered:  $\kappa_1^c$  and  $\kappa_2^c$  where  $c$  stands for connectivity. On the one hand, the normalised coordination, that is the number of Zn–N bonds relative to the total number of bonds, which is equal to the number of Zn atoms times 4 for perfect tetrahedral connectivity,  $4N_{\text{Zn}}$ , as would be the case in

Table 2: Cell parameters of a series of highly stable ZIF structures determined through geometry optimisations using nb-ZIF-FF (upright bold) and reference data from experimental (italic) and theoretical works.

		<i>a</i> / Å	<i>b</i> / Å	<i>c</i> / Å	$\alpha$ / °	$\beta$ / °	$\gamma$ / °
<i>zni</i>	nb-ZIF-FF	<b>23.28</b>	<b>23.28</b>	<b>12.64</b>	<b>90.01</b>	<b>90.00</b>	<b>90.00</b>
	MOF-FF <sup>61</sup>	23.23	23.23	12.79	90.00	90.00	90.00
	DFT <sup>61</sup>	23.35	23.35	12.56	90.00	90.00	90.00
	Exp. <sup>66</sup>	23.50	23.50	12.46	90.00	90.00	90.00
BCT ZIF-1	nb-ZIF-FF	<b>9.96</b>	<b>15.30</b>	<b>15.13</b>	<b>90.00</b>	<b>97.25</b>	<b>90.00</b>
	MOF-FF	10.09	14.55	15.91	90.00	117.00	90.00
	DFT <sup>65</sup>	9.74	15.39	15.18	90.00	98.55	90.00
	Exp. <sup>44</sup>	9.74	15.26	14.93	90.00	98.62	90.00
DFT ZIF-3	nb-ZIF-FF	<b>18.03</b>	<b>18.54</b>	<b>13.47</b>	<b>102.37</b>	<b>89.93</b>	<b>89.95</b>
	DFT <sup>65</sup>	18.96	18.96	16.77	90.00	90.00	90.00
	Exp. <sup>44</sup>	18.97	18.97	16.74	90.00	90.00	90.00
MER ZIF-10	nb-ZIF-FF	<b>26.92</b>	<b>26.92</b>	<b>20.16</b>	<b>90.00</b>	<b>90.02</b>	<b>89.78</b>
	DFT <sup>65</sup>	25.96	25.96	19.35	90.00	90.00	90.00
	Exp. <sup>67</sup>	27.37	27.37	18.58	90.00	90.00	90.00
GIS ZIF-6	nb-ZIF-FF	<b>19.34</b>	<b>19.34</b>	<b>20.14</b>	<b>90.00</b>	<b>90.00</b>	<b>90.00</b>
	MOF-FF	19.23	19.23	19.80	90.00	90.00	90.00
	DFT <sup>65</sup>	18.57	18.57	21.00	90.00	90.00	90.00
	Exp. <sup>44</sup>	18.52	18.52	20.25	90.00	90.00	90.00

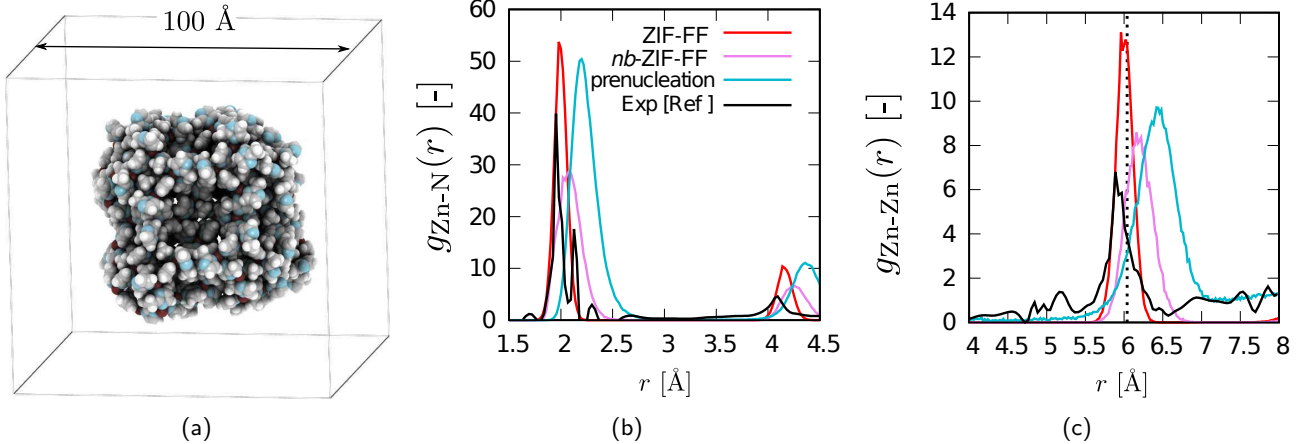


Figure 2: (a) Snapshot of a ZIF-8 cluster (the solvent was omitted for clarity). The core of the cluster remains stable but the connectivity of  $\text{MIm}^-$  and  $\text{Zn}^{2+}$  moieties at the surface changes over time. (b) Zn-N and (c) Zn-Zn radial distribution functions  $g(r)$ . ZIF-FF simulated, nb-ZIF-FF simulated and experimental<sup>68,69</sup> results are shown in red, pink and black lines respectively. The cyan solid lines show the corresponding  $g(r)$  of an under-coordinated cluster formed during the polymerisation simulations.

Table 3: Elastic constants of ZIF-8 and SALEM-2 computed with nb-ZIF-FF (upright bold), other force field-based or first principles calculations and experimental measurements (italic).

		$C_{11}$ / GPa	$C_{12}$ / GPa	$C_{44}$ / GPa
ZIF-8	nb-ZIF-FF (this work)	<b>12.67</b>	<b>4.00</b>	<b>2.915</b>
	ZIF-FF (this work)	9.33	6.45	1.37
	MOF-FF (by Dürholt <i>et al.</i> <sup>61</sup> )	8.54	6.55	0.62
	DFT (by Tan <i>et al.</i> <sup>70</sup> )	11.038	8.325	0.943
	Exp. (by Tan <i>et al.</i> <sup>70</sup> )	9.523	6.865	0.967
SALEM-2	nb-ZIF-FF	<b>6.333</b>	<b>3.775</b>	<b>2.6204</b>
	DFT by Zheng <i>et al.</i> <sup>71</sup>	8.949	7.59	2.36
	MOF-FF (by Dürholt <i>et al.</i> <sup>61</sup> )	6.65	4.95	1.12

perfectly coordinated bulk ZIF-8 crystals:

$$\kappa_1^c = \frac{1}{4N_{\text{Zn}}} \sum_{\substack{i \in \text{Zn atoms} \\ j \in \text{N atoms}}} \sigma_{ij} \quad (2)$$

$\sigma_{ij} = \sigma(r_{ij})$  is a switching function dependent of  $r_{ij}$  distance —i.e. equal to one when the corresponding Zn–N pair is connected and zero otherwise—. In order to make sure that the CV has continuous derivatives, we considered  $\sigma_{ij} = \exp(-(r_{ij}-d_0)^2/2r_0^2)$  as implemented in PLUMED with  $d_0 = 2.35 \text{ \AA}$  and  $r_0 = 0.2 \text{ \AA}$  (see Code 1 in Section S1 of the SI).<sup>74,75</sup>  $\kappa_1^c$  is zero when none of the Zn<sup>2+</sup> cations and ligands are coordinated —i.e. in the initial stage of Zn<sup>2+</sup> and MIm<sup>−</sup> mixing— and it takes the value of 1 for a fully-coordinated ZIF-8 crystal.

The second connectivity variable,  $\kappa_2^c$  is related to the clustering, it represents the ratio of Zn<sup>2+</sup> cations belonging to the largest connected cluster (see Code 2 in Section S1 of the SI). A cluster is defined as a continuous network formed by interconnected Zn<sup>2+</sup> and MIm<sup>−</sup> ligands. As such, this CV takes a value of zero at the initial stage of Zn<sup>2+</sup> and MIm<sup>−</sup> mixing and one when all the Zn<sup>2+</sup> cations belong to the same cluster. Both  $\kappa_1^c$  and  $\kappa_2^c$  were successfully used as CVs in an article by Tribello *et al.*<sup>76</sup>

We have also considered a subset of relevant order parameters. The density around a central  $i$ -atom and considering only the neighbours in a predefined environment  $\chi$  —e.g. , can be defined as

$$\rho_\chi(\mathbf{r}_i) = \sum_{j \in \chi} \exp\left(-\frac{|\mathbf{r}_i - \mathbf{r}_j|^2}{2\sigma^2}\right) \quad (3)$$

where  $i$  describes the neighbours in the environment  $\chi$  and  $\mathbf{r}_i$  are the coordinates of the neighbours with respect to the central atom. We considered the environmental similarity CV used by Piaggi and Parrinello,<sup>77</sup> which is based on this definition of local density and it is a generalised version of that proposed by Bartók *et al.*<sup>78,79</sup> This CV measures how an atomic environment  $\chi$  overlaps with a reference environment  $\chi_0$  with the following kernel function:

$$\begin{aligned} \kappa_{\chi_0}(\chi) &= \int d\mathbf{r} \rho_\chi(\mathbf{r}) \rho_{\chi_0}(\mathbf{r}) = \langle \rho_\chi | \rho_{\chi_0} \rangle \propto \\ &\propto \sum_{\substack{i \in \chi \\ j \in \chi_0}} \exp\left(-\frac{|\mathbf{r}_i - \mathbf{r}_j^0|^2}{2\sigma^2}\right) \end{aligned} \quad (4)$$

This quantity is measured for all Zn<sup>2+</sup> cations, for  $\chi$  and  $\chi_0$ , instantaneous and reference environments, respectively. For the ZIF-8 crystal thermal decomposition simulations, we have chosen the optimised positions of the Zn atoms at the ZIF-8 structure (*sod* topology) as the reference environment  $\chi_0$ . The *global* parameter,  $\omega_{\text{sod}}^0$ , for the whole system is constructed by calculating the ratio of Zn atoms with  $\kappa_{\text{sod}}(\chi) > \kappa^0$  (see Code 3 in Section S1 of the SI and Figure S2). For the simulations starting from the solvated Zn<sup>2+</sup> and MIm<sup>−</sup> moieties, the reference environment  $\chi_0$  was set as the first Zn–Zn tetrahedral environment (see Code 4 in Section S1 of the SI). In the same way than  $\omega_{\text{sod}}^0$ ,  $\omega_{\text{tet}}^0$  is constructed as

the ratio of Zn atoms than fulfil the reference tetrahedral environment (highlighted in yellow in Figure S2).

Finally, we tested the order parameters that were introduced by Steinhardt *et al.*<sup>80</sup> In essence, the orientational Steinhardt parameters,  $\{q_{lm}(\mathbf{r}_i)\}$ , can be understood as the projection of the “near neighbours”  $\sigma_\chi$  on the spherical harmonics around ( $r < r_c$ ) the central  $i$ -atom,

$$q_{lm}(i) = \langle \sigma | Y_m^l \rangle_i = \frac{1}{N_\chi(i)} \sum_{j \in \chi} \sigma(\mathbf{r}_{ij}) Y_{lm}(\mathbf{r}_{ij}) \quad (5)$$

for a generic  $l$  degree. This magnitude is an orientational order parameter and it is not invariant under rotation, so it cannot be used as such. Making use of the completeness of the spherical harmonics, a second-order invariant can be defined

$$\begin{aligned} Q_l(i) &\equiv \langle \sigma_\chi | \sigma_\chi \rangle_i^{1/2} := \\ &:= \left[ \frac{4\pi}{2l+1} \sum_{m=-l}^{+l} \sum_{j \in \chi} \langle \sigma | Y_{lm} \rangle_i \langle Y_{lm} | \sigma \rangle_j \right]^{1/2} \\ &= \left[ \frac{4\pi}{2l+1} \sum_{m=-l}^{+l} |q_{lm}|^2(i) \right]^{1/2} \end{aligned} \quad (6)$$

which is invariant under rotation and does not depend on the choice of reference frame. ten Wolde *et al.*<sup>81</sup> introduced the local-averaged Steinhardt parameters,

$$\overline{Q}_l(i) = \frac{1}{N_\chi(i)} \sum_{j \in \chi} \sigma(\mathbf{r}_{ij}) \sum_{m=-l}^{+l} q_{lm}^*(i) q_{lm}(j) \quad (7)$$

which measure how many of the atoms around the  $i$ -atom have a similar pattern,  $q_{lm}$  in their coordination spheres. The local-averaged Steinhardt parameters are still invariant under rotations and are recommended for distinguishing between liquid and solid phases.<sup>81,82</sup> Their value is large for atoms immersed in a crystalline phase and small for those belonging to the solvated ions phase. We have calculated the average of these parameters for all Zn atoms for  $l = 3, 4$ , and  $6$  as implemented in the PLUMED code (v2.7).<sup>74</sup> We have finally selected  $\omega_{Q_6}^0$ , the ratio of Zn atoms with  $\langle \overline{Q}_l \rangle > \langle \overline{Q}_l(\text{sod}) \rangle$  as a CV (see Code 5 in Section S1 of the SI).

## 2 Results and discussion

### 2.1 Selection of Collective Variables

We seek to study two transformations, one between the solvated Zn<sup>2+</sup> and MIm<sup>−</sup> moieties and the aggregate they form after polymerisation (early stages of ZIF-8 nucleation) and the other between the ZIF-8 crystal (Figure 3a right) and the liquid-like under-coordinated system that is obtained as a result of thermal decomposition at  $T > 600 \text{ K}$  (Figure 3a, left). In order to circumvent the energetic barriers that characterise these transformations we selected three CVs for our WT-MetaD simulations for each system. Two of them were used for both transformations:  $\kappa_1^c$ , the Zn–N connectivity ratio and  $\omega_{Q_6}^0$ , the ratio of Zn atoms with  $\langle \overline{Q}_6 \rangle > 0.8$  (see Figure S3). The third

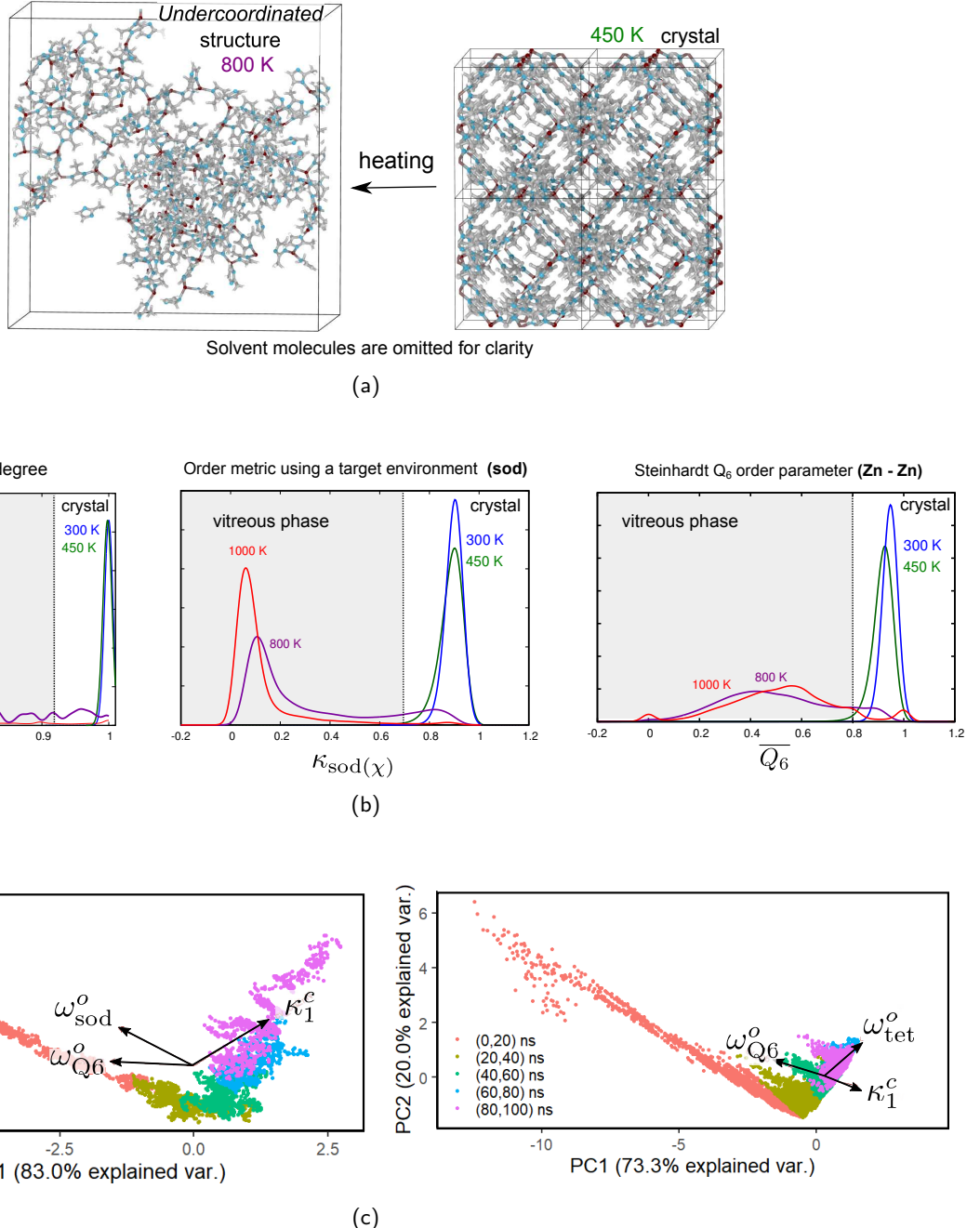


Figure 3: (a) Two snapshots taken from unbiased NPT MD simulations at (Left) 800 K, and (Right) 450 K. (b) Probability density functions for some CVs at 300 K to 1000 K: (Left) Zn-N coordination degree, (Middle), environmental similarity  $\kappa_{\text{sod}}(\chi)$  (critical value of  $\kappa^0 = 0.7$ ), and (Right) Steinhardt  $\langle Q_6 \rangle$  parameter (critical value of  $\langle Q_6^0 \rangle > 0.8$ ). (c) First two components of the principal component analysis performed on the values of all the explored CVs harvested along an unbiased MD simulation at  $T=800$  K starting from the ZIF-8 crystal (left) and  $T=298$  K starting from the uncoordinated solvated  $\text{Zn}^{2+}$  and  $\text{MIm}^-$  moieties. Both figures incorporate the projection of the selected CVs into the PC1-PC2 space.

CV was  $\omega_{\text{sod}}^o$ , the ratio of Zn atoms with  $\chi_{\text{sod}} > 0.7$  for the ZIF-8 crystal decomposition simulations and  $\omega_{\text{tet}}^o$ , the ratio of Zn atoms with  $\chi_{\text{tet}} > 8$  for the simulations of the early polymerisation of  $\text{Zn}^{2+}$  and  $\text{MIm}^-$  moieties. These CVs were selected so that one of them is strongly correlated with enthalpy ( $\kappa_1^c$ ) and the other two are related to order.

The time evolution of the two connectivity related CVs ( $\kappa_1^c$  and  $\kappa_2^c$ ) during the first nanosecond of a WT-MetaD simulation starting from the uncoordinated  $\text{Zn}^{2+}$  and  $\text{MIm}^-$  solvated moieties is shown in Figure S1. We found that these two CVs are highly correlated among themselves as well as with the enthalpy and the simulation box volume, so we decided to keep only  $\kappa_1^c$  as a representative for the connectivity/enthalpy group.

The order-related CVs that were selected for the early polymerisation simulations describe different aspects of local ordering. On the one hand,  $\omega_{Q_6}^o$  describes the symmetry of the arrangement of the first neighbour shell and also from the closest neighbouring atoms beyond the tetrahedron, it is based on spherical harmonics and not in reproducing a particular reference configuration. Among the three Steinhardt parameters-based CVs, we have selected  $\omega_{Q_6}^o$  instead of the  $Q_3$ - and  $Q_4$ - based CVs because it is the most commonly used in the literature to characterise solid/liquid states. On the other hand,  $\omega_{\text{tet}}^o$  focuses on reproducing the  $\text{Zn}(\text{MIm})_4^{2-}$  tetrahedron configuration by construction. For the ZIF-8 crystal decomposition study we kept  $\omega_{Q_6}^o$  because of its generic character and its ability to describe local order, but the targeted-structure CV  $\omega_{\text{tet}}^o$  was replaced by  $\omega_{\text{sod}}^o$  because in this case we aim to reproduce the sodalite crystal topology as reference configuration, and not only the tetrahedron formed by the first neighbours. In this sense,  $\omega_{\text{sod}}^o$  could be interpreted as a long-range order CV.

A basic pre-requisite for a CV to be appropriate for exploring the free energy surface that underlies a chemical transformation is that it needs to adopt different values for the states that are to be identified. To verify that this pre-requisite is fulfilled, we calculated the distribution of our chosen CVs for the different states described above. Figure 3b shows these distributions for the three selected CVs used to study the ZIF-8 crystal decomposition process. At low temperatures, the system exhibits the ZIF-8 crystal phase, while at high temperatures ( $T > 600$  K) it takes a liquid-like under-coordinated form. It is clear that the three CVs can differentiate the two states quite well. We established cutoff values for the CVs to define whether the system is crystalline or liquid-like in a binary fashion. These cutoffs are illustrated both in Figure 3b and S3 for the selected CVs and for some of the remaining CVs respectively. We have also performed the same analysis for simulations starting from the uncoordinated metal ions and ligands phase. All distributions are centred on zero at the beginning of the simulations and  $\kappa_1^c$  quickly rises as the nucleation process progresses.

To make sure that the selected CVs are not redundant, we run unbiased MD simulations for  $T = 300$  K, 450 K, 500 K, 600 K, 800 K and 1000 K lasting 3-4 ns in the NPT ensemble starting from a ZIF-8 crystal configuration filled with MeOH, and we calculated the values of the above

mentioned CVs along the simulation trajectory, as well as of volume and enthalpy. Another MD simulation was carried out at 298 K starting from the uncoordinated  $\text{MIm}^-$  ligands and  $\text{Zn}^{2+}$  cations immersed in MeOH for 100 ns to characterise the initial stages of the self-assembly process.

We then built a dataset combining all the harvested CV values and performed Principal Component Analysis (PCA). PCA consists on finding a new basis of orthogonal vectors in which the data are represented. These vectors  $\mathbf{v}_i$  are called the principal components, they are the eigenvectors of the covariance matrix and they are organised in such a way that the total variance of the data represented by vector  $\mathbf{v}_n$  is larger than that covered by vector  $\mathbf{v}_{n+1}$ . It is possible to profit from this property to choose only the first few principal components to represent the data, since they will allow to account for the largest part of the variance that characterises it. By performing PCA over the CVs values along the simulation, we can see how the system evolves in the PC space. Each point in the PC space represents the state of the system at a particular time. The euclidean distance between two points in the PC space can be used as a proxy for measuring how drastic has been the system's evolution between them. In addition, it is possible to measure the contribution of a particular CV to the evolution of the system in the PC space by computing the projection of the CV vector in the PC space.

The results of these analyses are shown in Figure 3c and Figure S6, where each point represents the position of the system in the PC1-PC2 space (the two principal components that best represent the dispersion of the data). At low temperature (300 K), we found that the system does not explore the PC space: the points are uniformly distributed in a small region of the PC space, and their distribution does not change with simulation time (see Figure S6). This observation is consistent with the direct inspection of the trajectory, which shows a stable ZIF-8 crystal all along the simulation. The degree of changes suffered by the system gradually increases with increasing temperature. The most drastic changes happen at  $T > 600$  K. Indeed, this also correlates with the visual inspection of the trajectory that shows that at higher temperatures, more  $\text{MIm}^-$  and  $\text{Zn}^{2+}$  moieties become dissociated, and at the limit of  $T > 600$  K we recover an under-coordinated, liquid-like system, as shown in Figure 3a left.

If we turn our attention to the evolution of the system in the PC space with time, we see that for the ZIF-8 crystal decomposition at high temperature (Figure 3c left panel) there is an initial transient period where the system suffers drastic changes (moves considerably along the PC space), mostly driven by the change in the cell volume produced by thermal expansion. After this period, which is quite short ( $\sim 500$  ps), the system evolution is drastically slowed down. This latter stage corresponds to the formation of the liquid-like under-coordinated phase. We note that temperature alone, with the consequent changes in the volume, is enough to drive the decomposition of the ZIF-8 crystal. The projection of our chosen CVs on the PC1-PC2 space are represented by vectors

that point to different directions in the PC space, thus proving that the selected CVs are not redundant as they allow to push the system into different realms in the PC space. The same behaviour is found for early polymerisation simulations starting from the solvated  $\text{MIm}^-$  and  $\text{Zn}^{2+}$  moieties (see Figure 3c right panel). Here, the selected CVs are also non redundant and we can also observe a fast initial period when the system undergoes important changes, associated with the polymerisation process and the formation of a highly-connected amorphous phase.

Finally, a system consisting of 2  $\text{Zn}$ , 4  $\text{MIm}^-$ , and 100 MeOH solvent molecules was prepared as a *toy* system to test that WT-MetaD explores the whole range of possible values of the CVs (see Figure S8). The system does indeed explore the full range of connectivity variables, proving that the simulation setup is suitable.

## 2.2 Free energy surface calculations

### 2.2.1 Early polymerisation of $\text{MIm}^-$ and $\text{Zn}^{2+}$ moieties

We further implemented our selected CVs into WT-MetaD simulations on the NPT ensemble starting from the solvated  $\text{Zn}^{2+}$  and  $\text{MIm}^-$  moieties to study the free energy surface and mechanistic details of the initial polymerisation stages of the ZIF-8 self-assembly.

We have performed a very short equilibration (less than 1 ps) because Zn-N bonds start forming early in the simulation as well as the first polymerisation events, such as the formation of  $\text{Zn}(\text{MIm})_2$  and  $\text{Zn}(\text{MIm})_3^-$  clusters. This is consistent with the observations by Filez *et al.*<sup>30</sup> concerning the early stages of formation of ZIF-67.

In the first 20 ps  $\sim 50\%$  of all possible Zn-N bonds have already been formed, and 85% of them within the first 150 ps. For  $t > 150$  ps,  $\kappa_1^c$  slowly increases until it reaches a plateau for a value that depends on the size of the system (see Figure S1). This behaviour can be ascribed to the fact that the size of the system is key to achieve the formation of a 3D fully-connected cluster. For the same composition (in terms of Zn atoms), if the total amount of solvent is less than a critical amount, percolated 1D, 2D or 3D-linked clusters are formed. Figure 4 illustrates the clusters that are formed in our WT-MetaD simulations. The low dimensionality clusters (rods, chains or planes) persist over time along all three simulation setups shown in Figure 4 (12  $\text{Zn}(\text{MIm})_2$  512 MeOH, 96  $\text{Zn}(\text{MIm})_2$  4096 MeOH and 324  $\text{Zn}(\text{MIm})_2$  13824 MeOH). The formation of low-dimensionality clusters has also been observed in previous simulation works<sup>31,32</sup> and could be in line with the idea of *aufbau* self-assembly mechanisms,<sup>84</sup> which postulate that 1D chains are first formed and associated to yield 2D planes that finally aggregate into 3D networks. Some of the clusters in Figure 4 percolate through the periodic boundary conditions, which is not desirable at this stage of the study as it implies an artificial stabilisation of the system. Indeed, such percolation phenomena may be favoured only because they lead to a huge drop in potential energy. To avoid unphysical effects, we work with relatively high MeOH/ $\text{Zn}(\text{MIm})_2$  ratios. However, a realistic study of the glass-to-crystalline transition must con-

sider percolation through realistic periodic boundary conditions, that cannot be achieved *via* an atomistic model such as the one we employ here due to restrictions in the cell size to perform the calculation within a reasonable computing time. It is thus necessary to work with larger systems, for example using coarse grained models and within a simulation ensemble that allows the number of solvent molecules to change, such as the constant chemical potential ensemble used by Karmakar *et al.*<sup>43</sup> Indeed, solvent-reactants interactions are crucial during the different stages of self-assembly, and large variations of local solvent densities at the different stages of the self-assembly process are to be expected. The dynamics and long-range connectivity of these low-dimensionality clusters will be further explored in future work combining *in situ* spectroscopy experiments with multiscale modelling techniques.

We have further studied the evolution of the clusters that are formed during these first polymerisation stages of the self-assembly process. In the first 50 - 200 ps there is a competition between different clusters to be the largest. The number of competing clusters depends on the size of the system. Clusters are created/destroyed by either one of two mechanisms: (i) direct aggregation/breakage of clusters or (ii) evaporation/condensation of moieties into/from other clusters. For low T systems ( $T = 298$  and 370 K), the smaller clusters evaporate after 200 ps and the remaining free  $\text{Zn}^{2+}$  and  $\text{MIm}^-$  moieties merge with the largest cluster (see Figure S7). However, the main growth mechanism is the direct aggregation of clusters.

The dominant cluster that is formed exhibits an amorphous aggregate topology, that could be assimilated to the amorphous highly-connected phase previously postulated as an intermediate species in the ZIF-8 self-assembly mechanism,<sup>51</sup> and that was also observed in the joint experimental/modelling work by Filez *et al.* for ZIF-67. This type of network is very resilient, its general appearance remains unchanged along the WT-MetaD simulations. Indeed, after 10-30 ns the local order-related CVs do fluctuate, but their mean values remain constant, and the nucleation process is stuck. This result may be an artefact of the simulation conditions, as the crystallisation process depends on the local concentration of reactants and solvent molecules near the nuclei interfaces. Since our simulations are run in the NPT ensemble (constant number of molecules), the lack of surface solvent may hinder the system's ability to crystallise further.

As a continuation of our study, we analysed the different species present in solution that drive the early stages of the nucleation process, the so-called pre-nucleation building units (PNBUs). Note that in our simulations  $\text{Zn}^{2+}$  cations tend to be tetracoordinated; which is not surprising since the force field is optimised for that purpose by using the CDA model, although the presence of tricoordinated cations is not negligible (see Figure 5). This is partly explained by the existence of surfaces that necessarily lowers the coordination of all species that constitute them, but also by the fact that the simulation is biased to explore different values of the Zn-N connectivity in the WT-MetaD (*via* the  $\kappa_1^c$  CV) and the cluster surface/volume ratio.

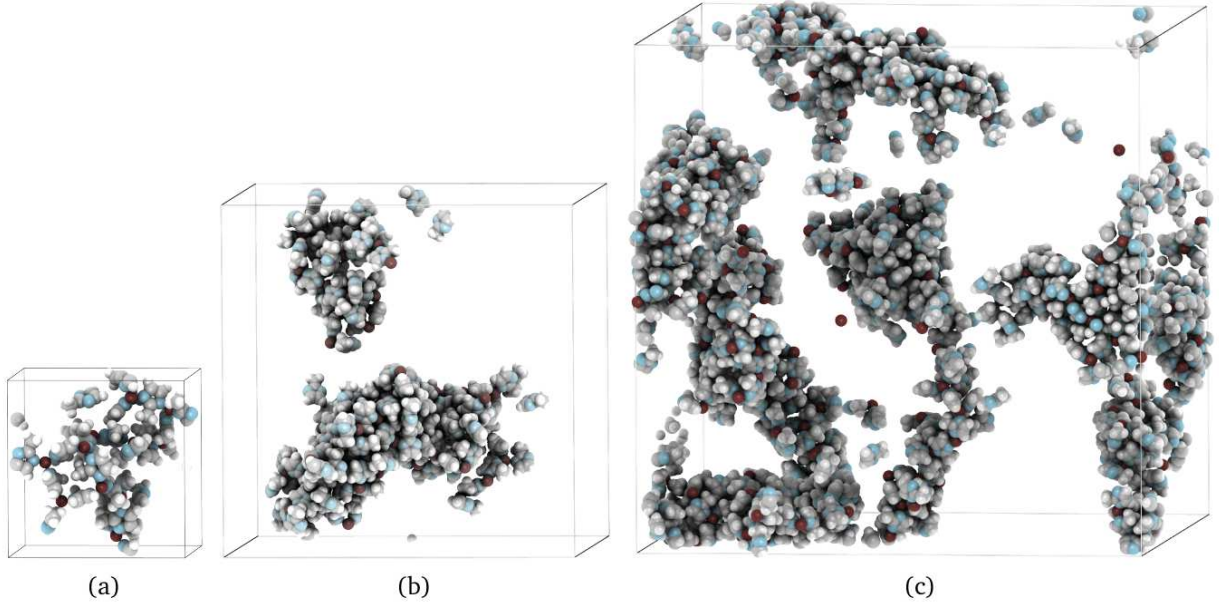


Figure 4: Snapshots for clusters with compositions: (a) 12  $\text{Zn}(\text{MIm})_2$  512 MeOH, (b) 96  $\text{Zn}(\text{MIm})_2$  4096 MeOH, and (c) 324  $\text{Zn}(\text{MIm})_2$  13824 MeOH. The  $\text{MeOH}/\text{ZnMIm}_2 = 128/3$  ratio is kept constant. Clusters were generated in WT-MetaD simulations at 400 K using  $\kappa_1^c$ ,  $\omega_{\text{sod}}^o$ , and  $\omega_{\text{Q6}}^o$  as CVs and the snapshots were taken at  $t = 20$  ns using the iRASPA software.<sup>83</sup> Dummy atoms and solvent molecules are omitted for clarity.

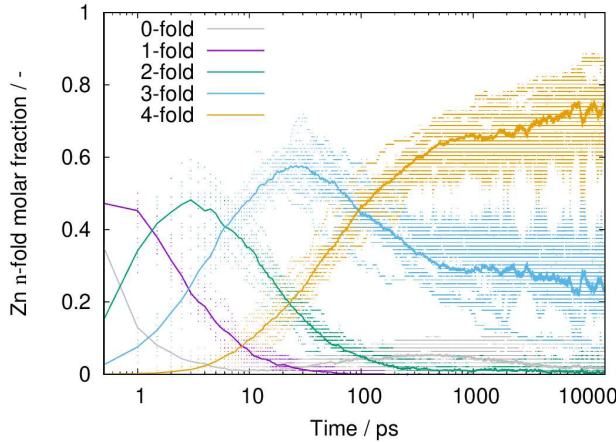


Figure 5: Population of  $n$ -fold coordinated  $\text{Zn}^{2+}$  cations in the simulation box over time for the 96  $\text{Zn}(\text{MIm})_2$  4096 MeOH system from WT-MetaD simulations over 12 walkers (same system as in Figure 4b).

We also observe the presence of free 4-fold connected  $\text{Zn}(\text{MIm})_4^{2-}$  and 3-fold connected  $\text{Zn}(\text{MIm})_3^-$  with half-lives of  $\sim 10$  ps, and free  $\text{MIm}^-$  anions with a half-life of  $\sim 1$  ps.  $\text{Zn}(\text{MIm})_x$  with  $x < 3$  are very rare for simulation times greater than 100 ps. Larger PNBUs corresponding to rings are also formed. We observed the formation of 4-membered rings comprising both tetra-coordinated and tri-coordinated metal cations. These rings are quite stable with half-lives of several nanoseconds ( $\sim 10$  ns). 5- and 6-membered rings are also present, both having similar stabilities ( $\sim 1$  ns). Direct inspection of the trajectory indicates that free  $\text{MIm}^-$  moieties act as "templating agents" in the formation of cages from the rings.

Finally, we computed the free energy surface in the CVs space for the early polymerisation of  $\text{Zn}^{2+}$  and  $\text{MIm}^-$  moieties, results are discussed in the next section.

## 2.2.2 ZIF-8 crystal thermal decomposition

In addition to exploring the first polymerisation stages of ZIF-8 formation we have explored the ZIF-8 crystal decomposition, as the opposite endpoint of the self-assembly process *via* WT-MetaD simulations. We considered three different amounts of adsorbed solvent, as shown in Table 1. We first calculated the free energy surfaces from the values of the CVs over time. The top panel in Figure 6 shows the three projections of the free energy surface for each pair of CVs for a  $2 \times 2 \times 2$  ZIF-8 supercell and 55.87 MeOH molecules per unit cell. The ZIF-8 crystal corresponds to the region labelled as (a) in the three plots. Along the WT-MetaD simulations, the order-related CVs are well explored. Indeed, the system can visit microstates with low CV values of about 0.15 - 0.2 for  $\omega_{\text{sod}}^o$  and  $\omega_{\text{Q6}}^o$ , represented by region (b) and then recover the initial state, in (c), thus proving that the WT-MetaD simulations are converged. The connectivity CV,  $\kappa_1^c$ , is however not explored to its full extent. Indeed, the decomposition does not reach to the uncoordinated  $\text{Zn}^{2+}$  and  $\text{MIm}^-$  solvated moieties, probably because of the limitations imposed by the fixed amount of solvent molecules during the simulation, as previously discussed. These microstates visited during the weak disassembly of ZIF-8, represented by the trajectory (a)  $\rightarrow$  (b)  $\rightarrow$  (c) are associated to free energy barriers of about 100  $\text{kJ mol}^{-1}$ . Microstate (c) exhibits almost the same values of the CVs as the crystalline microstate (a). The cleavage of 10% of the Zn-N links when passing from (a) to (b) generates

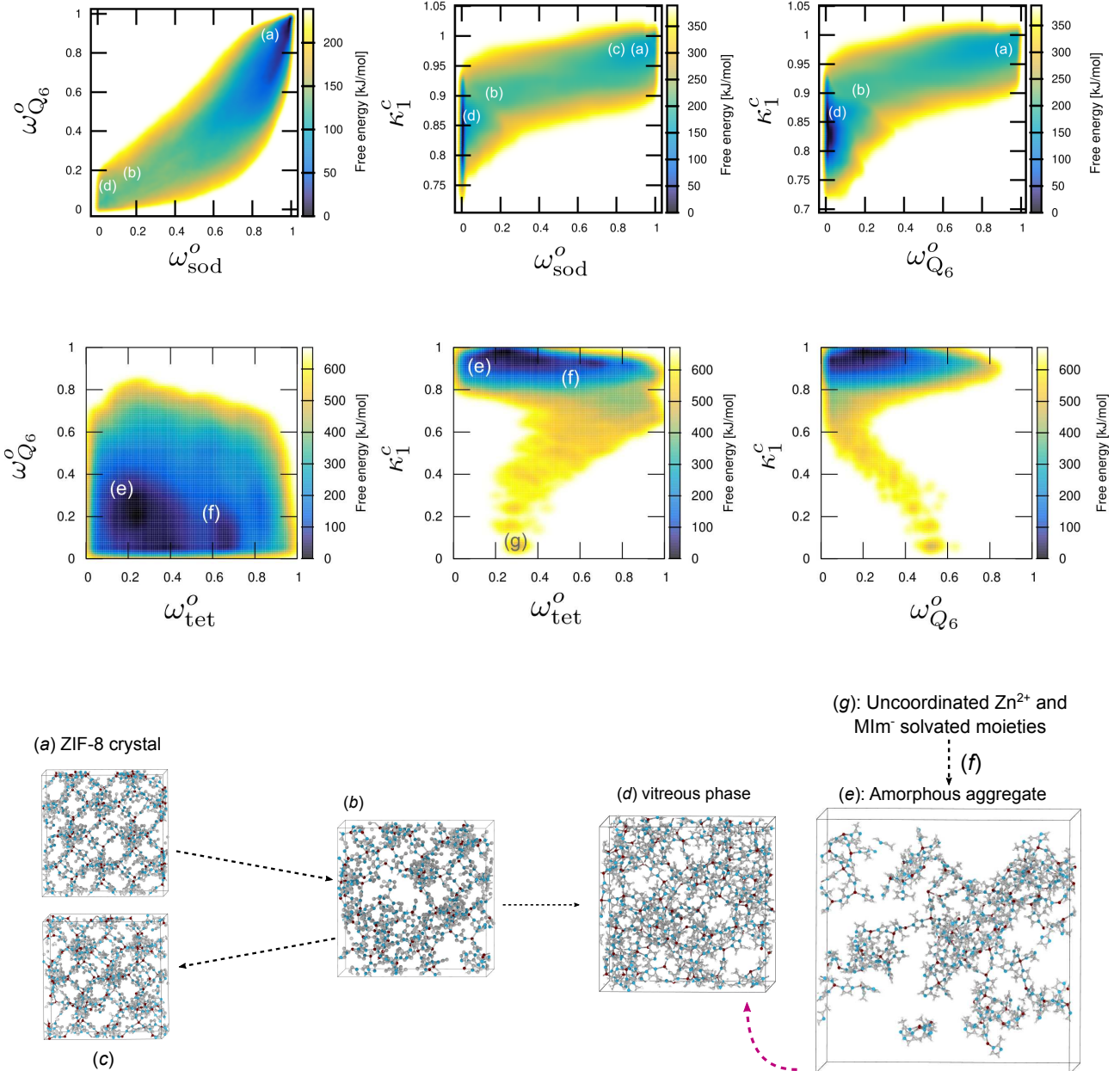


Figure 6: (Top) Three projections of the free energy surface for three CVs used in the simulations ( $\kappa_1^c$ ,  $\omega_{Q_6}^o$ , and  $\omega_{sod}^o$ ) starting from the ZIF-8 filled with methanol at 450 K, and (Middle) Three projections of the free energy surface for three CVs used in the simulations ( $\kappa_1^c$ ,  $\omega_{Q_6}^o$ , and  $\omega_{tet}^o$ ) starting from a supersaturated solution in methanol at 450 K. (Bottom) Snapshots of the trajectories for microstates which are representative of some of the phases visited along the simulations.

slightly larger porosities in the structure, which increase the solvent circulation. The possibility of coming back to the crystalline state seems to be conditioned to the exploration of the potential well region represented by label (d). This well is characterised by very low values of the CVs (from 0 to 0.15 for  $\omega_{Q_6}^o$ , and  $\omega_{\text{sod}}^o \sim 0$ ). The walkers that explore this region lose the ability to return to the perfect crystal configuration. This could be solved using a CV that better captures crystallinity. The microstates in (d) correspond to highly disordered systems that resemble the vitreous phase discussed above (very low  $\omega_{\text{sod}}^o$ , and  $\omega_{Q_6}^o$ ), with relatively high values of  $\kappa_1^c$ . Typical (a)-(d) microstates are illustrated at the bottom of Figure 6. Simulations containing less MeOH molecules (50 molecules per unit cell) exhibit a similar behaviour, but the free energy barriers were higher and although the system explored the (b) state, it was not able to return to the crystalline (a) phase. For an even lesser number of solvent molecules of 37.5 molecules per unit cell, the system was only able to explore the crystalline phase during a 100 ns-long simulation. These results highlight the crucial role of the solvent in the self-assembly process.

The central panel of Figure 6 depicts the three projections of the free energy surface of the early polymerisation process described in the previous section for comparison. These simulations start from the uncoordinated  $\text{Zn}^{2+}$  and  $\text{MIm}^-$  solvated moieties (labelled (g)). The trajectories of all the walkers quickly converge to state (f), which is characterised by a high Zn-N connectivity and a relatively high value of  $\omega_{\text{tet}}^o$ . The (f)  $\rightarrow$  (e) transformation is associated to an energy barrier of about  $100 \text{ kJ mol}^{-1}$ , and implies a reduction of the tetrahedral order and a rise of the Steinhardt order parameter. Both states, (f) and (e), turn out to be amorphous aggregates which are difficult to distinguish by simple visual inspection.

The connection between the amorphous aggregate state (e) and the vitreous state (d) cannot be made due to the very nature of the simulation performed (NPT MD). As the number of solvent molecules cannot be reduced, the system cannot percolate through the PBCs and become *crystalline*. As mentioned before, to model this part of the process one must enable changes in the number of solvent molecules with constant chemical potential, as proposed by Karmakar *et al.*<sup>85</sup>

### 3 Conclusions

In this work, we develop a computational methodology to unveil mechanistic details pertaining the two endpoints of ZIF-8 formation, namely, the  $\text{Zn}^{2+}$  -  $\text{MIm}^-$  moieties polymerisation (early stages of nucleation) and the thermal decomposition of a ZIF-8 crystal (associated with the late stages of the self-assembly process). We start by developing nb-ZIF-FF, an appropriate force field for this task, including (i) a physically sound model for taking into account the formation and breaking of metal-ligand connections *via* a Morse potential functional form, and (ii) cationic and anionic dummy atom models to mimic the spatial charge distribution of the metal cation in a ligands field. We have carefully validated our force field by checking the stability of different ZIFs and associated ag-

gregates and by computing radial distribution functions, cell parameters and elastic constants. Since nb-ZIF-FF successfully captures structure and energetics of all tested ZIFs, it can be applied to model the self-assembly and phase transformation of other ZIF polymorphs, as well as other studies that require including metal-ligand reactivity at system sizes larger than what can be achieved with *ab initio* resolution. We hope this contribution triggers further work in these directions. As a second step, we detail the collective variables that we select for our well-tempered metadynamics studies, we explain our rationale for choosing them and test their appropriateness and non-redundancy. We study the effect of temperature and of the size of the system in the simulation results. We explore the use of different solvents at the development part of our work and finally keep an explicit united atom model of methanol for the well-tempered metadynamics simulations. We discuss several tricks-of-the-trade related to modelling self-assembly processes.

Our well-tempered metadynamics simulations indicate that ZIF-8's self-assembly starts with a rapid increase of the Zn-N connectivity, up to 85% of the total possible bonds were formed within the first 150 ps. This stage is followed by the evaporation of small clusters into its constituents which are further combined with the largest clusters, while large clusters merge. Finally, a vitreous phase is formed, and the local order of the system gets stuck. Further progress in the self-assembly would require performing the simulation in a constant chemical potential ensemble, so that local solvent concentration fluctuations at the surfaces of the nuclei are possible and the system can percolate through the periodic boundaries. The pre-nucleation building units observed are single 4-fold and 3-fold connected  $\text{Zn}^{2+}$  cations with lifetimes in the order of picoseconds as well as 4-, 5- and 6-membered rings with lifetimes in the nanosecond realm. The free ligands act as "templating agents" for the formation of the sodalite cages. Finally, the free-energies of crystal decomposition and of the early polymerisation are explored. Thermal decomposition leads to the rapid formation of more disordered structures, and the stabilisation of an amorphous aggregate. Going from it to the vitreous phase formed in the early polymerisation simulations is not possible with the current methodology, but will be the object of further work.

Our work unveils molecular-level mechanistic details of the early and late stages of the ZIF-8 self-assembly process for the first time. This contributes to augmenting our fundamental understanding of the self-assembly processes, which is crucial in the rational design of new MOFs as well as for other materials. We also hope that this contribution will encourage further work in the simulation of other related reactive processes in solution.

### Author contribution

SRGB developed the force field, wrote the FORTRAN codes, set up the simulation framework (LAM-MPS/PLUMED/FORTRAN codes) and performed all unbiased MD simulations. RS designed the study and performed the PC analyses. SRGB and RS performed the

WT-MetaD simulations, discussed the results and wrote the manuscript.

## Supplementary Data

### Conflicts of interest

The authors declare that there is no conflict of interest.

### Acknowledgements

The authors thank G. Maurin, S. Hamad, and A. R. Ruiz-Salvador for valuable discussions at the initial stages of this work. We thank F. Abarca for his invaluable help in R coding. SRGB was supported by grants FJC2018-035697-I funded by MCIN/AEI/10.13039/501100011033 (Ministerio de Ciencia e Innovación; Agencia Estatal de Investigación) and POSTDOC\_21\_00069 funded by Consejería de Transformación Económica, Industria, Conocimiento y Universidades, Junta de Andalucía. This work was granted access to the HPC resources of CINES under the allocation A0090911989 made by GENCI. RS thanks the European Research Council for funding the ERC Starting Grant MAGNIFY (project 101042514) that will allow her to continue developing the computational modelling of MOFs self-assembly in solvothermal conditions.

### Supporting Information

The Supporting Information contains additional details pertaining the nb-ZIF-FF force field derivation, additional tests for its validation, FORTRAN codes for the generation of the LAMMPS input files and the initial dummy atoms positions, PLUMED input files as well as additional results from our simulations.

### S1 Plumed inputs

#### S1.1 Collective variables

We have used this code to calculate  $\kappa_1^c$ :

```

1 # Code 1
2 cn: COORDINATIONNUMBER ...
3 SPECIESA=Zn_atoms SPECIESB=N_atoms
4 SWITCH={GAUSSIAN R_0=0.02 D_0=0.325 D_MAX=0.35}
5 MEAN
6 ...
7 k_1: MATHEVAL ARG=cn.mean FUNC=x/4.0 PERIODIC=NO

```

and this code for  $\kappa_2^c$ :

```

1 # Code 2
2 cn: COORDINATIONNUMBER SPECIES=Zn_atoms ...
3 SWITCH={GAUSSIAN R_0=0.25 D_0=6.0 } MEAN LOWMEM
4 ...
5 # Construct a contact matrix between the atoms in the system
6 cm: CONTACT_MATRIX ATOMS=cn ...
7 SWITCH={GAUSSIAN R_0=0.25 D_0=6.0 }
8 ...
9 # Use depth first clustering to identify the sizes of the
10 # clusters
11 dfs: DFSCLUSTERING MATRIX=cm LOWMEM
12 # Calculate the number of atoms in the largest cluster
13 k_2: CLUSTER_NATOMS CLUSTERS=dfs CLUSTER=1

```

$\omega_{\text{sod}}^o$  is calculated from  $\kappa_{X_0}(x)$  and measures how similar the environment around Zn atoms is to that found in some reference crystal structure (see Figure S2 for the reference “sodalite” environment). In order to compute it, we used the CUSTOM keyword and provided the reference environment as a PDB file. We have used the Environment Finder app, developed by Piaggi<sup>86</sup> to determine the reference environments for the sod topology.

This is the code used to compute  $\omega_{\text{sod}}^o$ :

```

1 #Code 3
2 es_sod: ENVIRONMENTSIMILARITY ...
3 SPECIES=Zn_atoms
4 SIGMA=0.1
5 CRYSTAL_STRUCTURE=CUSTOM
6 # Degeneracy of each environment is 16
7 REFERENCE_1=env_1.pdb
8 REFERENCE_2=env_2.pdb
9 REFERENCE_3=env_3.pdb
10 REFERENCE_4=env_4.pdb
11 REFERENCE_5=env_5.pdb
12 REFERENCE_6=env_6.pdb
13 # Sum degeneracies 16*6 == 96 atoms of Zn
14 MEAN MORE_THAN={RATIONAL R_0=0.7 NN=24 MM=48}
15 ...
16 o_sod: MATHEVAL ARG=es_sod.morethan FUNC=x/96.0 PERIODIC=NO

```

This is the code used for computing  $\omega_{\text{tet}}^o$ :

```

1 #Code 4
2 es_tet: ENVIRONMENTSIMILARITY ...
3 SPECIES=Zn_atoms
4 SIGMA=0.5
5 CRYSTAL_STRUCTURE=CUSTOM
6 REFERENCE=env_00.pdb
7 MEAN MORE_THAN={RATIONAL R_0=8 NN=24 MM=48}
8 ...
9 # Degeneracy of the environment is 96
10 o_tet: MATHEVAL ARG=es_tet.morethan FUNC=x/96.0 PERIODIC=NO

```

This is the code used for computing  $\omega_{Q6}^o$

```

1 #Code 5
2 q6: Q6 SPECIES=Zn_atoms ...
3 SWITCH={GAUSSIAN R_0=0.02 D_0=0.72 D_MAX=0.74 }
4 LOWMEM MEAN VMEAN
5 ...
6 lq6: LOCAL_Q6 SPECIES=q6 ...

```

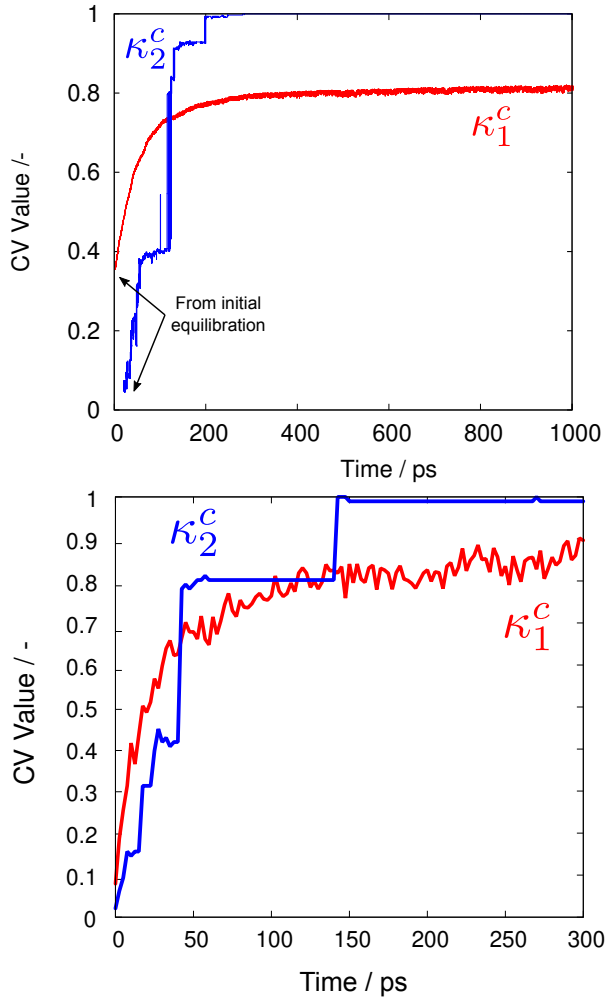


Figure S1: Time evolution of the CVs  $\kappa_1^c$  and  $\kappa_2^c$  at (top) 370 K for 96 Zn(Im)₂ 4096 MeOH composition within the first nanosecond, and (bottom) 450 K for 324 Zn(Im)₂ 13824 MeOH within the first 0.3 nanoseconds.

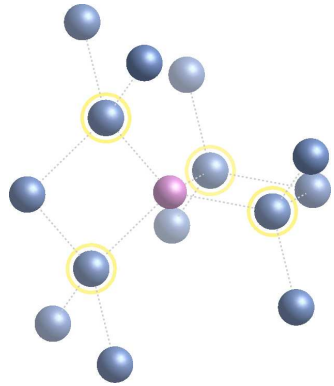


Figure S2: Reference environments. The Zn atoms in a SOD topology (ZIF-8) within a radius of  $r < 7 \text{ \AA}$  of a random Zn atom are coloured in blue, while the central atom is shown in pink. This set of atoms constitutes the  $X_{\text{sod}}$  environment. All Zn atoms are equivalent. The Zn atoms closest to the central Zn atom, which correspond to the  $X_{\text{tet}}$  environment, are highlighted in yellow.

```

7 SWITCH={GAUSSIAN R_0=0.02 D_0=0.72 D_MAX=0.74 }
8 LOWMEM MEAN MORE_THAN={RATIONAL R_0=0.8 NN=24 MM=48}
9 ...
10 o_q6: MATHEVAL ARG=1q6.morethan FUNC=x/96.0 PERIODIC=NO

```

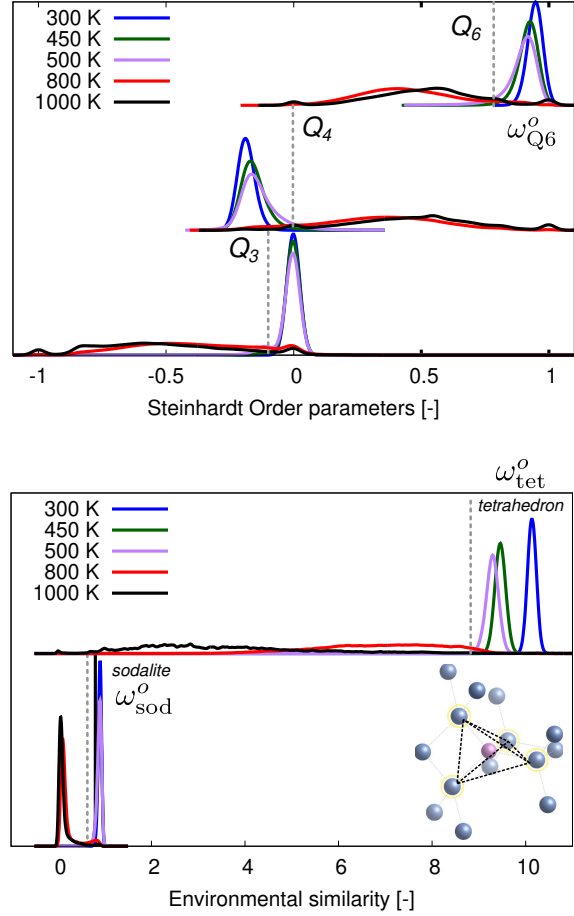


Figure S3: Probability density functions for different locally averaged Steinhardt parameter variables (Top)  $Q_3$ ,  $Q_4$ , and  $Q_6$  (see Code 6, line 6 for the local average), and (Bottom)  $\omega_{\text{sod}}^o$ , and  $\omega_{\text{tet}}^o$  for all temperatures explored.

## S1.2 Analysis

This code was used to calculate the curves in Figure 5.

```

1 # Code 6
2 # f(x)=exp(- (x-D_0)**2/(2*R_0**2)) ; D_0=2.2 ; R_0=0.1
3 cn: COORDINATIONNUMBER SPECIESA=Zn_atoms SPECIESB=N_atoms ...
4 SWITCH={GAUSSIAN R_0=0.01 D_0=0.325 D_MAX=0.35} MEAN
   LOWMEM
5 ...
6 # 1-fold
7 fcm1: MFILTER_MORE DATA=cn ...
   SWITCH={GAUSSIAN D_0=0.99 R_0=0.01 D_MAX=1.0}
8 ...
9 cm1: CONTACT_MATRIX ATOMS=fcm1 ...
   SWITCH={GAUSSIAN R_0=0.01 D_0=0.325 D_MAX=0.35}
10 ...
11 dfs1: DFSCLUSTERING MATRIX=cm1 LOWMEM
12 nclust1: CLUSTER_DISTRIBUTION CLUSTERS=dfs1 ...
   TRANSFORM={GAUSSIAN D_0=0.99 R_0=0.01 D_MAX=1.0}
13 MORE_THAN={GAUSSIAN D_0=0.99 R_0=0.01 D_MAX=1}
14 ...
15 # 2-fold
16 fcm2: MFILTER_MORE DATA=cn ...
   SWITCH={GAUSSIAN D_0=1.99 R_0=0.01 D_MAX=2.0}
17 ...
18 cm2: CONTACT_MATRIX ATOMS=fcm2 ...
   SWITCH={GAUSSIAN R_0=0.01 D_0=0.325 D_MAX=0.35}

```

```

24 ...
25 dfs2: DFSCLUSTERING MATRIX=cm2 LOWMEM
26 nclust2: CLUSTER_DISTRIBUTION CLUSTERS=dfs2 ...
27     TRANSFORM={GAUSSIAN D_0=1.99 R_0=0.01 D_MAX=2.0}
28     MORE_THAN={GAUSSIAN D_0=0.99 R_0=0.01 D_MAX=1}
29 ...
30 # 3-fold
31 fcm3: MFILTER_MORE DATA=cn ...
32     SWITCH={GAUSSIAN D_0=2.99 R_0=0.01 D_MAX=3.0}
33 ...
34 cm3: CONTACT_MATRIX ATOMS=fcm3 ...
35     SWITCH={GAUSSIAN R_0=0.01 D_0=0.325 D_MAX=0.35}
36 ...
37 dfs3: DFSCLUSTERING MATRIX=cm3 LOWMEM
38 nclust3: CLUSTER_DISTRIBUTION CLUSTERS=dfs3 ...
39     TRANSFORM={GAUSSIAN D_0=2.99 R_0=0.01 D_MAX=3.0}
40     MORE_THAN={GAUSSIAN D_0=0.99 R_0=0.01 D_MAX=1}
41 ...
42 # 4-fold
43 fcm4: MFILTER_MORE DATA=cn ...
44     SWITCH={GAUSSIAN D_0=3.99 R_0=0.01 D_MAX=4.0}
45 ...
46 cm4: CONTACT_MATRIX ATOMS=fcm4 ...
47     SWITCH={GAUSSIAN R_0=0.01 D_0=0.325 D_MAX=0.35}
48 ...
49 dfs4: DFSCLUSTERING MATRIX=cm4 LOWMEM
50 nclust4: CLUSTER_DISTRIBUTION CLUSTERS=dfs4 ...
51     TRANSFORM={GAUSSIAN D_0=3.99 R_0=0.01 D_MAX=4.0}
52     MORE_THAN={GAUSSIAN D_0=0.99 R_0=0.01 D_MAX=1}
53 ...

```

**Keywords:** COORDINATIONNUMBER, ENVIRONMENT-SIMILARITY, Q6, and LOCAL\_Q6

## S2 nb-ZIF Force Field

A first version of the Morse potential was obtained by fitting the harmonic potential (Zn-N) to a Morse function plus the sum of the electrostatic potentials of the nearest neighbours (atoms and dummy particles). This second contribution is an underestimated approximation of the total electrostatic interaction in the periodic system, so the contribution of the Morse potential is overestimated in this initial version. Therefore, despite the excellent agreement between the two curves shown in Figure S4, the potential obtained in this way does not provide good results, since it underestimates the effect of the charges and the periodic system collapses.

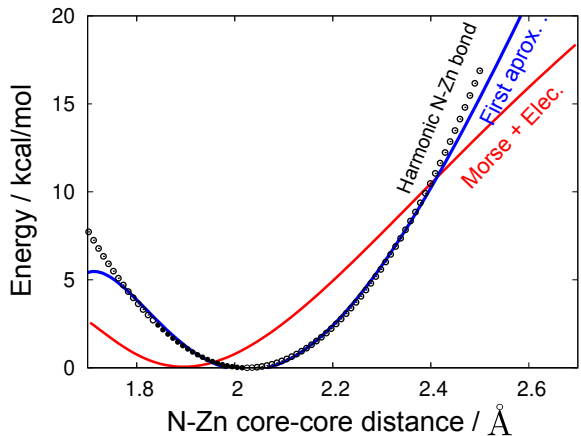


Figure S4: Comparison between the Morse potential fit for the dispersion interactions and the harmonic potential used as a basis.

In a second step, the obtained Morse potential was refined with the GULP program,<sup>87</sup> and used as an input to generate a force field refined to reproduce the experimental crystal structures (cell parameters and atomic coordinates) of ZIF-8 and SALEM-2 (both SOD topology with  $\text{MIm}^-$  and  $\text{Im}^-$  ligands, respectively).

For the GULP calculations, we have used the following keywords: fit comp prop simul opti, which allow us to simultaneously fit the potential and optimise the coordinates of the ZIF-8, SALEM-2, and *zni* structures. We applied this procedure to optimise the parameters that are related to Zn-N bond cleavage and associated angles, and left all other ZIF-FF parameters unchanged.

Three sets of charges for the CDA model (Zn and N atoms) were tested for the cationic/anionic dummy atom models: 1),  $\delta_c^+ = \delta_s^+ = Q_{\text{Zn}}/5$  for Zn-dummies, and  $q_s^N = Q_{\text{N}}$  for N-dummies, 2),  $\delta_c^+ = Q_{\text{Zn}}/2$ ,  $\delta_s^+ = Q_{\text{Zn}}/8$  for Zn-dummies, and  $q_s^N = Q_{\text{N}}$  for N-dummies, and 3)  $\delta_c^+ = Q_{\text{Zn}}/2$ ,  $\delta_s^+ = Q_{\text{Zn}}/8$  for Zn-dummies, and  $q_s^N = Q_{\text{N}} + 0.02e$ , and  $q_s^N = -0.02e$  for N-dummies. The Morse potential values were optimised in accordance with these charge sets. We tested these sets by running an NPT Unbiased-MD of the ZIF-8 crystal phase. Set (2) was chosen since it was the one that best reproduced ZIF-8's radial distribution functions. Finally, the Zn-N Morse potential was re-optimised for this set.

For calculations involving  $\text{Im}^-$  instead of  $\text{MIm}^-$  ligands (*zni* and other ZIFs mentioned in the main manuscript),

Table S1: Cell parameters of ZIF-8 and SALEM-2 calculated with nb-ZIF-FF (upright bold) and reference data from both experimental measurements (italic) and calculations from other published works.

		<i>a</i> / Å	<i>b</i> / Å	<i>c</i> / Å	$\alpha$ / °	$\beta$ / °	$\gamma$ / °
SALEM-2	nb-ZIF-FF	<b>16.85</b>	<b>16.85</b>	<b>16.85</b>	<b>90.00</b>	<b>90.00</b>	<b>90.00</b>
	MOF-FF <sup>61</sup>	16.97	16.97	16.97	90.00	90.00	90.00
	DFT <sup>65</sup>	17.02	17.02	17.02	90.00	90.00	90.00
	Exp. <sup>88</sup>	<i>16.83</i>	<i>16.83</i>	<i>16.83</i>	<i>90.00</i>	<i>90.00</i>	<i>90.00</i>
ZIF-8	nb-ZIF-FF	<b>16.99</b>	<b>16.99</b>	<b>16.99</b>	<b>90.00</b>	<b>90.00</b>	<b>90.00</b>
	MOF-FF	17.08	17.08	17.08	90.00	90.00	90.00
	DFT <sup>61</sup>	17.03	17.03	17.03	90.00	90.00	90.00
	Exp. <sup>44</sup>	16.99	16.99	16.99	90.00	90.00	90.00

we slightly modified the ZIF-FF to adapt it to the  $\text{Im}^-$  ligand: a) the total charge of the aromatic  $\text{C}(C_1) +$  methyl group ( $C_3 + 2H_3$ ) connected to the aromatic  $\text{C}(C_1)$  in  $\text{MIm}^-$  was considered equal to the charge of the aromatic  $C_4$  and the  $H_4$  connected to it in  $\text{Im}^-$ , b) the charge of  $H_4$  was considered equal to the charge of  $H_2$ , and c) changes in intramolecular interactions were considered as parsimonious as possible —*i.e.* assigning equal parameters to similar bonds, bends, dihedrals, etc. In addition, the interaction of the EPS solvent atoms with the Zn atom was tuned to obtain the same equilibrium distances as in the case of the TraPPE methanol model.

The LAMMPS inputs files (force field) for the *zni* and ZIF-8 simulations have been uploaded as supplementary material.

Table S2: Energies of a series of ZIFs relative to the energy of the *zni* topology per Zn atom ( $\Delta E = \frac{E}{Z_{\text{Zn}}} - \frac{E^{\text{zni}}}{Z_{\text{Zn}^{\text{zni}}}}$  (eV)) computed by DFT calculations from Lewis *et al.*<sup>65</sup> and by nb-ZIF-FF (this work).

Topology/MOF	$\Delta E_{\text{DFT}}$ [eV]	$\Delta E_{\text{nb-ZIF-FF}}$ [eV]
<i>zni</i>	0.0	0.0
<i>cag</i> /ZIF-4	0.0756	0.0519
BCT/ZIF-1	0.0921	0.1687
DFT/ZIF-3	0.1362	0.1978
SOD/SALEM-2	0.1328	0.2553
MER/ZIF-10	0.1246	0.2600
GIS/ZIF-6	0.1405	0.2911

To avoid energy divergences in the integration of the MD simulations due to the strong electrostatic interactions, we have added a wall potential,  $\propto r^{-12}$ , at very short distances between dummy atoms.

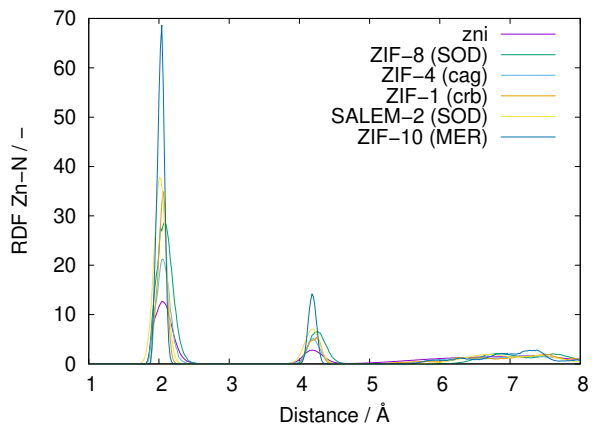


Figure S5: Zn–N radial distribution functions for several crystalline structures calculated with the nb-ZIF-FF (final set of charges) from unbiased MD simulations at 300 K.

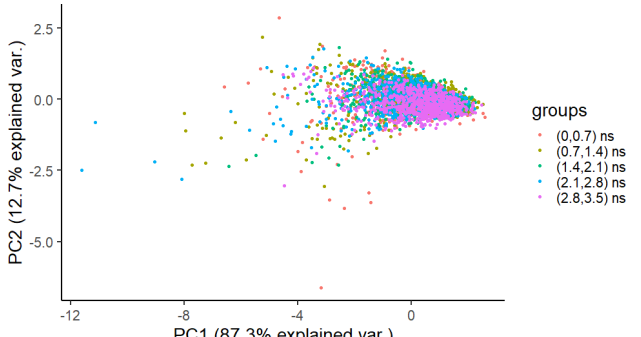


Figure S6: Time evolution of collective variables data plotted in the space defined by the two first principal components for a 300 K unbiased MD run starting from the ZIF-8 crystal.

### S3 Well-Tempered Metadynamics

For simulations starting from ZIF-8, we biased the crystal formation/destruction to be aligned with the simulation box using the following parameter defined by Piaggi and Parrinello:<sup>77</sup>

$$s_c = \frac{\hat{Q}_6 - \hat{Q}_6^I}{\hat{Q}_6^s - \hat{Q}_6^I} - \frac{\bar{\kappa} - \bar{\kappa}^I}{\bar{\kappa}^s - \bar{\kappa}^I} \quad (\text{S1})$$

where  $\hat{Q}_6$  is the norm of the mean complex vector  $q_{6m}$  defined in Equation 5, and  $\bar{\kappa}$  is defined in Equation 4. . .<sup>I</sup>

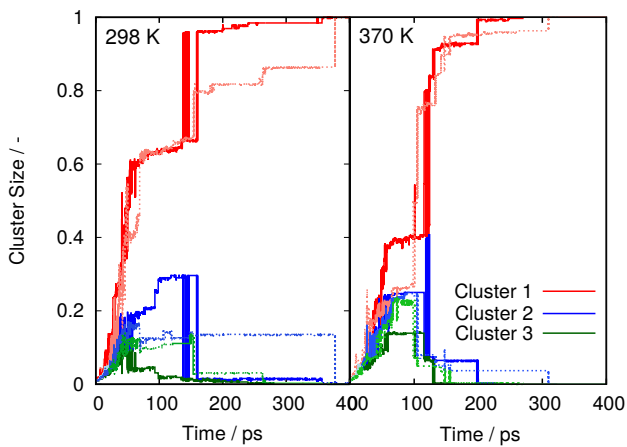


Figure S7: Time evolution of the size (the ratio of the number of  $\text{Zn}^{2+}$  belonging to the tagged cluster relative to the total number of  $\text{Zn}^{2+}$ ) for the three largest clusters at 298 and 370 K. Two independent runs were performed for each system (solid and dotted lines).

and  $\dots^s$  marks the averaged values for liquid (uncoordinated) and solid states, respectively. This parameter is constrained with a harmonic potential ( $u_{\text{wall}}$ , see Code 7).

```

1 # Code 7
2 meta: METAD ARG=k_1,o_sod,o_q6 ...
3   PACE=200 HEIGHT=0.5 SIGMA=0.02,0.02,0.02
4   BIASFACTOR=20 TEMP=450.0 FILE=HILLS WALKERS_MPI
5 ...
6 #           q6.vmean
7 # crystal_q6: 0.54166, crystal_es: 0.839854
8 # liquid:      0                  0
9 # vitreous:   0.0453738      0.550492
10 sc: MATHEVAL ARG=q6_ZnZn.vmean,es_sod.mean FUNC=(x-0.1)
11   / (0.54166-0.1)-y PERIODIC=NO
12 uwall: UPPER_WALLS ARG=cv_1,cv_2,cv_3,cv_4,sc ...
13   AT=1,1,1,1,0.2 KAPPA=1,1,1,1 EXP=2,2,2,2,2
14 ...
15 lwall: LOWER_WALLS ARG=cv_1,cv_2,cv_3,cv_4 ...
16   AT=0,0,0,0 KAPPA=1,1,1 EXP=2,2,2,2
17 ...
18 bias: COMBINE ARG=*.bias PERIODIC=NO

```

## References

- Xuan Zhang, Zhijie Chen, Xinyao Liu, Sylvia L. Hanna, Xingjie Wang, Reza Taheri-Ledari, Ali Maleki, Peng Li, and Omar K. Farha. A historical overview of the activation and porosity of metal-organic frameworks. *Chem. Soc. Rev.*, 49(20):7406–7427, 2020. DOI: 10.1039/d0cs00997k.
- Pei-Long Wang, Lin-Hua Xie, Elizabeth A. Joseph, Jian-Rong Li, Xiao-Ou Su, and Hong-Cai Zhou. Metal-organic frameworks for food safety. *Chem. Rev.*, 119(18):10638–10690, 2019. DOI: 10.1021/acs.chemrev.9b00257.
- Sureshkumar Kempahumakkagari, Kowsalya Vellingiri, Akash Deep, Eilhann E. Kwon, Nanthi Bolan, and Ki-Hyun Kim. Metal-organic framework composites as electrocatalysts for electrochemical sensing applications. *Coord. Chem. Rev.*, 357:105 – 129, 2018. DOI: 10.1016/j.ccr.2017.11.028. ISSN 0010-8545.
- Mónica Giménez-Marqués, Tania Hidalgo, Christian Serre, and Patricia Horcajada. Nanostructured metal-organic frameworks and their bio-related applications. *Coord. Chem. Rev.*, 307:342 – 360, 2016. DOI: 10.1016/j.ccr.2015.08.008. ISSN 0010-8545. Chemistry and Applications of Metal Organic Frameworks.
- Sarita Dhaka, Rahul Kumar, Akash Deep, Mayur B. Kurade, Sang-Woo Ji, and Byong-Hun Jeon. Metal-organic frameworks (mofs) for the removal of emerging contaminants from aquatic environments. *Coord. Chem. Rev.*, 380:330 – 352, 2019. DOI: 10.1016/j.ccr.2018.10.003. ISSN 0010-8545.
- Meili Ding, Robinson W. Flraig, Hai-Long Jiang, and Omar M. Yaghi. Carbon capture and conversion using metal-organic frameworks and mof-based materials. *Chem. Soc. Rev.*, 48: 2783–2828, 2019. DOI: 10.1039/C8CS00829A.
- Guillaume Maurin, Christian Serre, Andrew Cooper, and Gérard Férey. The new age of MOFs and of their porous-related solids. *Chem. Soc. Rev.*, 46(11):3104–3107, 2017. DOI: 10.1039/c7cs90049j.
- Meili Ding, Robinson W. Flraig, Hai-Long Jiang, and Omar M. Yaghi. Carbon capture and conversion using metal-organic frameworks and MOF-based materials. *Chem. Soc. Rev.*, 48 (10):2783–2828, 2019. DOI: 10.1039/c8cs00829a.
- Yao Du, Hui Su, Teng Fei, Baoping Hu, Jichuan Zhang, Shenghua Li, Siping Pang, and Fude Nie. Structure–property relationship in energetic cationic metal–organic frameworks: New insight for design of advanced energetic materials. *Cryst. Growth Des.*, 18(10):5896–5903, August 2018. DOI: 10.1021/acs.cgd.8b00640.
- Germán E. Gomez, Elena V. Brusau, Joaquín Sacanell, Galo J. A. A. Soler Illia, and Griselda E. Narda. Insight into the metal content-structure-property relationship in lanthanide metal-organic frameworks: Optical studies, magnetism, and catalytic performance. *Eur. J. Inorg. Chem.*, 2018(20-21): 2452–2460, May 2018. DOI: 10.1002/ejic.201701474.
- Wei Li, Xiaoxiao Xia, Meng Cao, and Song Li. Structure–property relationship of metal–organic frameworks for alcohol-based adsorption-driven heat pumps via high-throughput computational screening. *J. Mater. Chem.A*, 7(13):7470–7479, 2019. DOI: 10.1039/c8ta07909a.
- Stefano Dissegna, Pia Vervoorts, Claire L. Hobday, Tina Dürren, Dominik Daisenberger, Andrew J. Smith, Roland A. Fischer, and Gregor Kieslich. Tuning the mechanical response of metal-organic frameworks by defect engineering. *J. Am. Chem. Soc.*, 140(37):11581–11584, August 2018. DOI: 10.1021/jacs.8b07098.
- David S. Sholl and Ryan P. Lively. Defects in metal-organic frameworks: Challenge or opportunity? *J. Phys. Chem. Lett.*, 6(17):3437–3444, August 2015. DOI: 10.1021/acs.jpclett.5b01135.

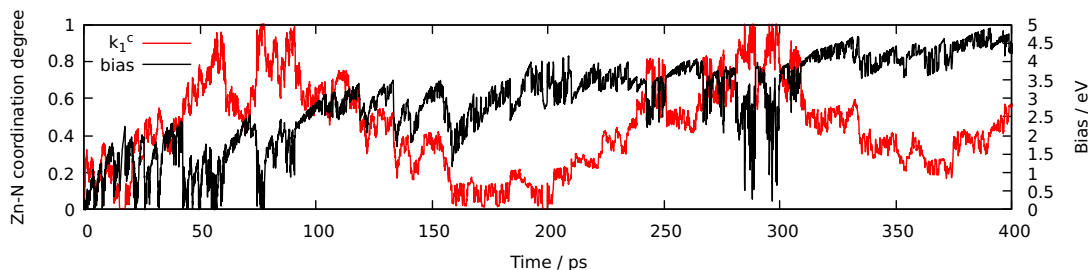


Figure S8:  $\kappa_1^c$  (biased CV) and bias potential of the WT-MetaD over time for a toy system formed by 2  $\text{Zn}^{2+}$  cations and 4  $\text{MIm}^-$  anions plus 100 MeOH solvent molecules.

[14] Marco Taddei. When defects turn into virtues: The curious case of zirconium-based metal-organic frameworks. *Coord. Chem. Rev.*, 343:1–24, July 2017. DOI: 10.1016/j.ccr.2017.04.010.

[15] Mohadeseh Safaei, Mohammad Mehdi Foroughi, Nasser Ebrahimpoor, Shohreh Jahani, Ali Omidi, and Mehrdad Khatami. A review on metal-organic frameworks: Synthesis and applications. *TrAC - Trends Anal. Chem.*, 118:401–425, September 2019. DOI: 10.1016/j.trac.2019.06.007.

[16] Vincent Guillerm and Daniel Maspoch. Geometry mismatch and reticular chemistry: Strategies to assemble metal-organic frameworks with non-default topologies. *J. Am. Chem. Soc.*, 141(42):16517–16538, September 2019. DOI: 10.1021/jacs.9b08754.

[17] Hao Jiang, Jiangtao Jia, Aleksander Shkurenko, Zhijie Chen, Karim Adil, Youssef Belmabkhout, Lukasz J. Weselinski, Ayalew H. Assen, Dong-Xu Xue, Michael O’Keeffe, and Mohamed Eddaoudi. Enriching the reticular chemistry repertoire: Merged nets approach for the rational design of intricate mixed-linker metal-organic framework platforms. *J. Am. Chem. Soc.*, 140(28):8858–8867, June 2018. DOI: 10.1021/jacs.8b04745.

[18] Ting Wang, En Lin, Yun-Lei Peng, Yao Chen, Peng Cheng, and Zhenjie Zhang. Rational design and synthesis of ultramicroporous metal-organic frameworks for gas separation. *Coord. Chem. Rev.*, 423:213485, November 2020. DOI: 10.1016/j.ccr.2020.213485.

[19] Ralph Freund, Stefano Canossa, Seth M. Cohen, Wei Yan, Hexiang Deng, Vincent Guillerm, Mohamed Eddaoudi, David G. Madden, David Fairen-Jimenez, Hao Lyu, Lauren K. Macreadie, Zhe Ji, Yuanyuan Zhang, Bo Wang, Frederik Haase, Christof Wöll, Orysia Zaremba, Jacopo Andreo, Stefan Wuttke, and Christian S. Dierckx. 25 years of reticular chemistry. *Angew. Chem. Int. Ed.*, March 2021. DOI: 10.1002/anie.202101644.

[20] Hao Jiang, Dalal Alezi, and Mohamed Eddaoudi. A reticular chemistry guide for the design of periodic solids. *Nat. Rev. Mater.*, March 2021. DOI: 10.1038/s41578-021-00287-y.

[21] Suzy Surblé, Franck Millange, Christian Serre, Gérard Férey, and Richard I. Walton. An EXAFS study of the formation of a nanoporous metal-organic framework: evidence for the retention of secondary building units during synthesis. *Chem. Commun.*, (14):1518, 2006. DOI: 10.1039/b600709k.

[22] Maryam Shoaei, Michael W. Anderson, and Martin P. Atfield. Crystal growth of the nanoporous metal-organic framework HKUST-1 revealed by in situ atomic force microscopy. *Angew. Chem. Int. Ed.*, 47(44):8525–8528, October 2008. DOI: 10.1002/anie.200803460.

[23] Janosch Cravillon, Roman Nayuk, Sergej Springer, Armin Feldhoff, Klaus Huber, and Michael Wiebcke. Controlling zeolitic imidazolate framework nano- and microcrystal formation: Insight into crystal growth by time-resolved in situ static light scattering. *Chem. Mater.*, 23(8):2130–2141, 2011. DOI: 10.1021/cm103571y.

[24] Martin P. Atfield and Pablo Cubillas. Crystal growth of nanoporous metal organic frameworks. *Dalton Trans.*, 41(14):3869–3878, 2012. DOI: 10.1039/c2dt12006b.

[25] Maarten G. Goesten, Eli Stavitski, Jana Juan-Alcañiz, Alberto Martínez-Joaristi, Andrei V. Petukhov, Freek Kapteijn, and Jorge Gascon. Small-angle x-ray scattering documents the growth of metal-organic frameworks. *Catal. Today*, 205:120–127, April 2013. DOI: 10.1016/j.cattod.2012.08.044.

[26] Joseph P. Patterson, Patricia Abellán, Michael S. Denny, Chiwoo Park, Nigel D. Browning, Seth M. Cohen, James E. Evans, and Nathan C. Gianneschi. Observing the growth of metal-organic frameworks by in situ liquid cell transmission electron microscopy. *J. Am. Chem. Soc.*, 137(23):7322–7328, 2015. DOI: 10.1021/jacs.5b00817.

[27] Krista S. Walton. Movies of a growth mechanism. *Nature*, 523(7562):535–536, 2015. DOI: 10.1038/523535a.

[28] Stijn Van Cleuvenbergen, Zachary J. Smith, Olivier Deschaume, Carmen Bartic, Sebastian Wachsmann-Hogiu, Thierry Verbiest, and Monique A. van der Veen. Morphology and structure of zif-8 during crystallisation measured by dynamic angle-resolved second harmonic scattering. *Nat. Commun.*, 9(1):3418, 2018. DOI: 10.1038/s41467-018-05713-4.

[29] Daniel Saliba, Manal Ammar, Moustafa Rammal, Mazen Al-Ghoul, and Mohamad Hmadeh. Crystal growth of zif-8, zif-67, and their mixed-metal derivatives. *J. Am. Chem. Soc.*, 140 (5):1812–1823, 2018. DOI: 10.1021/jacs.7b11589.

[30] Matthias Filez, Chiara Caratelli, Miguel Rivera-Torrente, Francesco Muniz-Miranda, Max Hoek, Maarten Altelaar, Albert J.R. Heck, Veronique Van Speybroeck, and Bert M. Weckhuysen. Elucidation of the pre-nucleation phase directing metal-organic framework formation. *Cell Rep. Physical Science*, 2(12):100680, dec 2021. DOI: 10.1016/j.xcrp.2021.100680.

[31] Makoto Yoneya, Seiji Tsuzuki, and Masaru Aoyagi. Simulation of metal-organic framework self-assembly. *Phys. Chem. Chem. Phys.*, 17(14):8649–8652, 2015. DOI: 10.1039/c5cp00379b.

[32] Debasmita Biswal and Peter G. Kusalik. Probing molecular mechanisms of self-assembly in metal-organic frameworks. *ACS Nano*, 11(1):258–268, December 2016. DOI: 10.1021/acsnano.6b05444.

[33] Debasmita Biswal and Peter G. Kusalik. Molecular simulations of self-assembly processes in metal-organic frameworks: Model dependence. *J. Chem. Phys.*, 147(4):044702, July 2017. DOI: 10.1063/1.4994700.

[34] Yuan-Ping Pang. Novel zinc protein molecular dynamics simulations: Steps toward antiangiogenesis for cancer treatment. *J. Mol. Model.*, 5(10):196–202, October 1999. DOI: 10.1007/s008940050119.

[35] Yamil J. Colón, Ashley Z. Guo, Lucas W. Antony, Kyle Q. Hoffmann, and Juan J. de Pablo. Free energy of metal-organic framework self-assembly. *J. Chem. Phys.*, 150(10):104502, March 2019. DOI: 10.1063/1.5063588.

[36] Loukas Kollias, David C. Cantu, Marcus A. Tubbs, Roger Rousseau, Vassiliki-Alexandra Glezakou, and Matteo Salvalaglio. Molecular level understanding of the free energy landscape in early stages of metal–organic framework nucleation. *J. Am. Chem. Soc.*, 141(14):6073–6081, March 2019. DOI: 10.1021/jacs.9b01829.

[37] Alessandro Laio and Michele Parrinello. Escaping free-energy minima. *Proc. Natl. Acad. Sci. U.S.A.*, 99(20):12562–12566, 2002. DOI: 10.1073/pnas.202427399. ISSN 0027-8424.

[38] David C. Cantu, B. Peter McGrail, and Vassiliki-Alexandra Glezakou. Formation mechanism of the secondary building unit in a chromium terephthalate metal–organic framework. *Chem. Mater.*, 26(22):6401–6409, October 2014. DOI: 10.1021/cm5027859.

[39] Alessandro Barducci, Giovanni Bussi, and Michele Parrinello. Well-tempered metadynamics: A smoothly converging and tunable free-energy method. *Phys. Rev. Lett.*, 100(2), January 2008. DOI: 10.1103/physrevlett.100.020603.

[40] Giovanni Bussi and Davide Branduardi. Free-energy calculations with metadynamics: Theory and practice. In *Rev. Comput. Chem.*, pages 1–49. John Wiley & Sons, Inc, May 2015.

[41] D. Quigley and P.M. Rodger. A metadynamics-based approach to sampling crystallisation events. *Mol. Simul.*, 35(7): 613–623, April 2009. DOI: 10.1080/08927020802647280.

[42] Yue-Yu Zhang, Haiyang Niu, GiovanniMaria Piccini, Dan Mendels, and Michele Parrinello. Improving collective variables: The case of crystallization. *J. Chem. Phys.*, 150(9): 094509, March 2019. DOI: 10.1063/1.5081040.

[43] Tarak Karmakar, Michele Invernizzi, Valerio Rizzi, and Michele Parrinello. Collective variables for the study of crystallisation. *Mol. Phys.*, 119(19–20), March 2021. DOI: 10.1080/00268976.2021.1893848.

[44] Kyo Sung Park, Zheng Ni, Adrien P. Côté, Jae Yong Choi, Rudan Huang, Fernando J. Uribe-Romo, Hee K. Chae, Michael O’Keeffe, and Omar M. Yaghi. Exceptional chemical and thermal stability of zeolitic imidazolate frameworks. *Proc. Natl. Acad. Sci. U.S.A.*, 103(27):10186–10191, June 2006. DOI: 10.1073/pnas.0602439103.

[45] Binling Chen, Zhuxian Yang, Yanqiu Zhu, and Yongde Xia. Zeolitic imidazolate framework materials: recent progress in synthesis and applications. *J. Mater. Chem. A*, 2:16811–16831, 2014. DOI: 10.1039/C4TA02984D.

[46] Denise Zacher, Osama Shekhah, Christof Wöll, and Roland A. Fischer. Thin films of metal–organic frameworks. *Chem. Soc. Rev.*, 38:1418–1429, 2009. DOI: 10.1039/B805038B.

[47] Yichang Pan, Yunyang Liu, Gaofeng Zeng, Lan Zhao, and Zhiping Lai. Rapid synthesis of zeolitic imidazolate framework-8 (zif-8) nanocrystals in an aqueous system. *Chem. Commun.*, 47:2071–2073, 2011. DOI: 10.1039/C0CC05002D.

[48] Janosch Cravillon, Simon Münzer, Sven-Jare Lohmeier, Armin Feldhoff, Klaus Huber, and Michael Wiebcke. Rapid room-temperature synthesis and characterization of nanocrystals of a prototypical zeolitic imidazolate framework. *Chem. Mater.*, 21:1410–1412, 2009. DOI: 10.1021/cm900166h.

[49] Xuhui Feng, Ting Wu, and Moises A. Carreon. Synthesis of ZIF-67 and ZIF-8 crystals using DMSO (dimethyl sulfoxide) as solvent and kinetic transformation studies. *J. Cryst. Growth*, 455:152–156, December 2016. DOI: 10.1016/j.jcrysgro.2016.10.016.

[50] Xiao-Gang Wang, Qian Cheng, Yun Yu, and Xian-Zheng Zhang. Controlled nucleation and controlled growth for size predictable synthesis of nanoscale metal–organic frameworks (mofs): A general and scalable approach. *Angew. Chem. Int. Ed.*, 57(26):7836–7840, 2018. DOI: 10.1002/anie.201803766.

[51] Surendar R. Venna, Jacek B. Jasinski, and Moises A. Carreon. Structural evolution of zeolitic imidazolate framework-8. *J. Am. Chem. Soc.*, 132(51):18030–18033, December 2010. DOI: 10.1021/ja109268m.

[52] Steve Plimpton. Fast parallel algorithms for short-range molecular dynamics. *J. Comput. Phys.*, 117(1):1–19, mar 1995. DOI: 10.1006/jcph.1995.1039.

[53] Elijah Polak and Gerard Ribière. Note sur la convergence de méthodes de directions conjuguées. *Rev. Fr. Autom., Inf. Rech. Opér., Sér.: Rouge*, 3(1):35–43, 1969.

[54] Erik Bitzek, Pekka Koskinen, Franz Gähler, Michael Moseler, and Peter Gumbsch. Structural relaxation made simple. *Phys. Rev. Lett.*, 97(17), oct 2006. DOI: 10.1103/physrevlett.97.170201.

[55] David Dubbeldam, Sofía Calero, Donald E. Ellis, and Randall Q. Snurr. RASPA: molecular simulation software for adsorption and diffusion in flexible nanoporous materials. *Mol. Simul.*, 42(2):81–101, February 2015. DOI: 10.1080/08927022.2015.1010082.

[56] Zhongqiao Hu, Liling Zhang, and Jianwen Jiang. Development of a force field for zeolitic imidazolate framework-8 with structural flexibility. *J. Chem. Phys.*, 136(24):244703, June 2012. DOI: 10.1063/1.4729314.

[57] Liling Zhang, Zhongqiao Hu, and Jianwen Jiang. Sorption-induced structural transition of zeolitic imidazolate framework-8: A hybrid molecular simulation study. *J. Am. Chem. Soc.*, 135(9):3722–3728, February 2013. DOI: 10.1021/ja401129h.

[58] Bin Zheng, Marco Sant, Pierfranco Demontis, and Giuseppe B. Suffratti. Force field for molecular dynamics computations in flexible ZIF-8 framework. *J. Phys. Chem. C*, 116(1):933–938, January 2012. DOI: 10.1021/jp209463a.

[59] Xuanjun Wu, Jin Huang, Weiquan Cai, and Mietek Jaroniec. Force field for ZIF-8 flexible frameworks: atomistic simulation of adsorption, diffusion of pure gases as CH4, h2, CO2 and n2. *RSC Adv.*, 4(32):16503–16511, 2014. DOI: 10.1039/c4ra00664j.

[60] Tingting Weng and J. R. Schmidt. Flexible and transferable ab initio force field for zeolitic imidazolate frameworks: ZIF-FF. *J. Phys. Chem. A*, 123(13):3000–3012, March 2019. DOI: 10.1021/acs.jpca.8b12311.

[61] Johannes P. Dürholt, Guillaume Fraux, François-Xavier Coudert, and Rochus Schmid. Ab initio derived force fields for zeolitic imidazolate frameworks: MOF-FF for ZIFs. *J. Chem. Theory Comput.*, 15(4):2420–2432, March 2019. DOI: 10.1021/acs.jctc.8b01041.

[62] Sudi Jawahery, Nakul Rampal, Seyed Mohamad Moosavi, Matthew Witman, and Berend Smit. Ab initio flexible force field for metal–organic frameworks using dummy model coordination bonds. *J. Chem. Theory Comput.*, 15(6):3666–3677, May 2019. DOI: 10.1021/acs.jctc.9b00135.

[63] Vu Nguyen and Michael Grünwald. Microscopic origins of poor crystallinity in the synthesis of covalent organic framework COF-5. *J. Am. Chem. Soc.*, 140(9):3306–3311, February 2018. DOI: 10.1021/jacs.7b12529.

[64] Becky L. Eggemann, Amara J. Sunnarborg, Hudson D. Stern, Andrew P. Bliss, and J. Ilja Siepmann. An online parameter and property database for the trappe force field. *Mol. Simul.*, 40(1-3):101–105, 2014. DOI: 10.1080/08927022.2013.842994.

[65] Dewi W. Lewis, A. Rabdel Ruiz-Salvador, Ariel Gómez, L. Marleny Rodríguez-Albelo, François-Xavier Coudert, Ben Slater, Anthony K. Cheetham, and Caroline Mellot-Draznieks. Zeolitic imidazole frameworks: structural and energetics trends compared with their zeolite analogues. *CrystEngComm*, 11(11):2272, 2009. DOI: 10.1039/b912997a.

[66] Elinor C. Spencer, Ross J. Angel, Nancy L. Ross, Brian E. Hanson, and Judith A. K. Howard. Pressure-induced cooperative bond rearrangement in a zinc imidazolate framework: A high-pressure single-crystal x-ray diffraction study. *J. Am. Chem. Soc.*, 131(11):4022–4026, March 2009. DOI: 10.1021/ja808531m.

[67] Joseph R. Ramirez, Haiyang Yang, Christopher M. Kane, Amanda N. Ley, and K. Travis Holman. Reproducible synthesis and high porosity of mer-zn(im)2 (ZIF-10): Exploitation of an apparent double-eight ring template. *J. Am. Chem. Soc.*, 138(37):12017–12020, September 2016. DOI: 10.1021/jacs.6b06375.

[68] Shuai Cao, Thomas D. Bennett, David A. Keen, Andrew L. Goodwin, and Anthony K. Cheetham. Amorphization of the prototypical zeolitic imidazolate framework ZIF-8 by ball-milling. *Chem. Commun.*, 48(63):7805, 2012. DOI: 10.1039/c2cc33773h.

[69] Thomas D. Bennett, Shuai Cao, Jin Chong Tan, David A. Keen, Erica G. Bithell, Patrick J. Beldon, Tomislav Friscic, and Anthony K. Cheetham. Facile mechanosynthesis of amorphous zeolitic imidazolate frameworks. *J. Am. Chem. Soc.*, 133(37):14546–14549, September 2011. DOI: 10.1021/ja206082s.

[70] Jin-Chong Tan, Bartolomeo Civalleri, Chung-Cherng Lin, Loredana Valenzano, Raimondas Galvelis, Po-Fei Chen, Thomas D. Bennett, Caroline Mellot-Draznieks, Claudio M. Zicovich-Wilson, and Anthony K. Cheetham. Exceptionally low shear modulus in a prototypical imidazole-based metal-organic framework. *Phys. Rev. Lett.*, 108(9), February 2012. DOI: 10.1103/physrevlett.108.095502.

[71] Bin Zheng, Yihan Zhu, Fang Fu, Lian Li Wang, Jinlei Wang, and Huijing Du. Theoretical prediction of the mechanical properties of zeolitic imidazolate frameworks (ZIFs). *RSC Adv.*, 7(66):41499–41503, 2017. DOI: 10.1039/c7ra07242b.

[72] Paolo Raiteri, Alessandro Laio, Francesco Luigi Gervasio, Cristian Micheletti, and Michele Parrinello. Efficient reconstruction of complex free energy landscapes by multiple walkers metadynamics. *J. Phys. Chem. B*, 110(8):3533–3539, 2006. DOI: 10.1021/jp054359r.

[73] Janosch Cravillon, Christian A. Schröder, Helge Bux, André Rothkirch, Jürgen Caro, and Michael Wiebcke. Formate modulated solvothermal synthesis of zif-8 investigated using time-resolved *in situ* x-ray diffraction and scanning electron microscopy. *CrystEngComm*, 14:492–498, 2012. DOI: 10.1039/C1CE06002C.

[74] The PLUMED consortium. Promoting transparency and reproducibility in enhanced molecular simulations. *Nat. Methods*, 16(8):670–673, July 2019. DOI: 10.1038/s41592-019-0506-8.

[75] Giovanni Bussi and Gareth A. Tribello. Analyzing and biasing simulations with PLUMED. In *Methods Mol. Biol.*, pages 529–578. Springer New York, 2019.

[76] Gareth A. Tribello, Federico Giberti, Gabriele C. Sosso, Matteo Salvalaglio, and Michele Parrinello. Analyzing and driving cluster formation in atomistic simulations. *J. Chem. Theory Comput.*, 13(3):1317–1327, February 2017. DOI: 10.1021/acs.jctc.6b01073.

[77] Pablo M. Piaggi and Michele Parrinello. Calculation of phase diagrams in the multithermal-multibaric ensemble. *J. Chem. Phys.*, 150(24):244119, June 2019. DOI: 10.1063/1.5102104.

[78] Albert P. Bartók, Risi Kondor, and Gábor Csányi. On representing chemical environments. *Phys. Rev. B*, 87(18), May 2013. DOI: 10.1103/physrevb.87.184115.

[79] Sandip De, Albert P. Bartók, Gábor Csányi, and Michele Ceriotti. Comparing molecules and solids across structural and alchemical space. *Phys. Chem. Chem. Phys.*, 18(20):13754–13769, 2016. DOI: 10.1039/c6cp00415f.

[80] Paul J. Steinhardt, David R. Nelson, and Marco Ronchetti. Bond-orientational order in liquids and glasses. *Phys. Rev. B*, 28(2):784–805, July 1983. DOI: 10.1103/physrevb.28.784.

[81] Pieter Rein ten Wolde, Maria J. Ruiz-Montero, and Daan Frenkel. Numerical calculation of the rate of crystal nucleation in a lennard-jones system at moderate undercooling. *J. Chem. Phys.*, 104(24):9932–9947, June 1996. DOI: 10.1063/1.471721.

[82] Wolfgang Lechner and Christoph Dellago. Accurate determination of crystal structures based on averaged local bond order parameters. *J. Chem. Phys.*, 129(11):114707, September 2008. DOI: 10.1063/1.2977970.

[83] David Dubbeldam, Sofía Calero, and Thijs J.H. Vlugt. iR-ASPA: GPU-accelerated visualization software for materials scientists. *Mol. Simul.*, 44(8):653–676, January 2018. DOI: 10.1080/08927022.2018.1426855.

[84] R. Murugavel, M. G. Walawalkar, Meenakshi Dan, H. W. Roesky, and C. N. R. Rao. Transformations of molecules and secondary building units to materials: a bottom-up approach. *Acc. Chem. Res.*, 37(10):763–774, October 2004. DOI: 10.1021/ar040083e. URL <https://doi.org/10.1021/ar040083e>.

[85] Tarak Karmakar, Pablo M. Piaggi, and Michele Parrinello. Molecular dynamics simulations of crystal nucleation from solution at constant chemical potential. *J. Chem. Theory Comput.*, 15(12):6923–6930, October 2019. DOI: 10.1021/acs.jctc.9b00795.

[86] Pablo Piaggi. Environment finder: A tool for finding and analyzing atomic environments in crystal structures. <https://doi.org/10.5281/zenodo.4746325>, 2021.

[87] Julian D. Gale and Andrew L. Rohl. The general utility lattice program (GULP). *Mol. Simul.*, 29(5):291–341, May 2003. DOI: 10.1080/0892702031000104887.

[88] Olga Karagiariidi, Marianne B. Lalonde, Wojciech Bury, Amy A. Sarjeant, Omar K. Farha, and Joseph T. Hupp. Opening ZIF-8: A catalytically active zeolitic imidazolate framework of sodalite topology with unsubstituted linkers. *J. Am. Chem. Soc.*, 134(45):18790–18796, October 2012. DOI: 10.1021/ja308786r.